Extrinsic Calibration of a Vision Sensor Mounted on a Robot

Ching-Cheng Wang

Abstract— **A vision sensor is mounted on a robot to detect surrounding objects. Its mounting position and orientation must be identified, resulting in an extrinsic calibration problem. This paper presents three classes of extrinsic calibration procedures. All use closed-form solutions. The class A calibration procedure requires a reference object at a precalibrated location. The class B calibration procedure takes advantage of a robot's mobility. It requires a reference frame but not precalibration. The class C procedure, by taking full advantage of both robot mobility and dexterity, requires no reference object but the simplest one—a visible point. In simulation studies, the class A, B, and C calibration procedures have produced estimates successfully converging to true extrinsic parameter values. Except the class A calibration procedure, which yields biased results unless the precalibration is free from errors, field experiments have been carried out for class B and C calibration procedures. For comparison, two existing B-type calibration methods, namely, those of Tsai and Lenz and Shiu and Ahmad, have also been tested with real data. Individually, each method has achieved consistent results. Collectively, their results appear to be comparable. Standard deviations obtained by class B and the Tsai–Lenz methods have been smaller than those of the Shiu–Ahmad method. On average, the Tsai–Lenz method has achieved the smallest standard deviations.**

I. Introduction

VISION sensors capable of finding the position and orientation of an object are mounted on a robot manipulator to enhance tracking accuracy, versatile robot-operator communication, and intelligent task control [5], [6], [12], [14], [15], [19], [23], [24], [26], [27]. However, visual information is of no use unless the sensor is calibrated. The calibration of a vision camera consists of intrinsic and extrinsic calibrations. The intrinsic calibration determines the geometric and optical characters of the camera, whereas the extrinsic calibration identifies its mounting position.

The $\{ip\}$-, $\{s\}$- and $\{n\}$-frames of Fig. 1 represent the coordinate frames of the image plane, the camera, and the mounted link, respectively, where the origin of the $\{s\}$-frame is located at the lens light center. The extrinsic calibration determines the position and orientation of the $\{s\}$-frame as described in the $\{n\}$-frame, a total of six parameters. The intrinsic parameters consist of the pixel dimensions d_x and d_y, the uncertainty scale factor s_x, the coordinates of the image center c_x and c_y, the effective focal length f, the lens distortion coefficients, and the orientation of the $\{ip\}$-frame as described in the $\{s\}$-frame [2], [3], [16], [38], a total of $(9 + n_d)$ parameters, where n_d is the number of

Manuscript received March 29, 1989; revised July 15, 1991.

The author is with the Department of Industrial Engineering and Information Systems, Northeastern University, Boston, MA 02115.

IEEE Log Number 9106454.

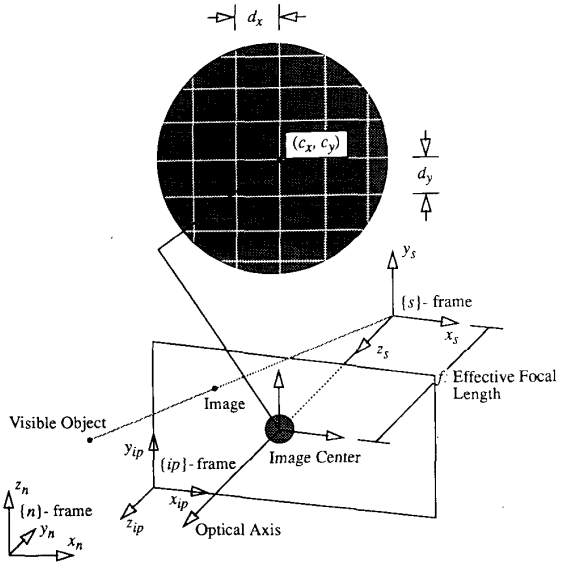

Fig. 1. Frames for describing intrinsic and extrinsic homogeneous transforms.

significant radial and tangential lens distortion coefficients. Various methods, e.g., [1], [4], [7]–[11], [13], [17], [18], [20]–[22], [28], [30]–[32], have been explored to calibrate subsets of intrinsic and extrinsic parameters.

Intrinsic and extrinsic parameters can be calibrated separately. Tsai [33] and Wang and Lai [37] separately reported intrinsic calibration methods. Tsai and Lenz [34] and Shiu and Ahmad [29] independently explored extrinsic calibration methods. Shiu and Ahmad rigorously rearranged the calibration problem into a set of quadratically constrained linear regression equations, which was then resolved using the least squares fit solution. Tsai and Lenz, via closed-form solutions, derived algorithms of simplicity, efficiency, and accuracy.

The extrinsic calibration has to be carried out at the robot site. This paper presents three classes of extrinsic calibration procedures to substantiate a complete treatment. All use closed-form solutions. The requirements of reference objects are listed in Table I.

The homogeneous transform has equivalent representations which offer convenient language in different respects. They are addressed in the next section. Then Sections III to V present the class A, B, and C calibration procedures, respectively. Section VI reports implementation results. The summary and discussions are contained in Section VII.

TABLE I
REFERENCE OBJECTS OF CLASS A, B, AND C CALIBRATION PROCEDURES

Procedure	Requirements of Reference Objects
A	The reference object has its position and orientation precalibrated.
B	The reference object is well structured but not precalibrated.
C	The reference object is a single point. Its position is not precalibrated.

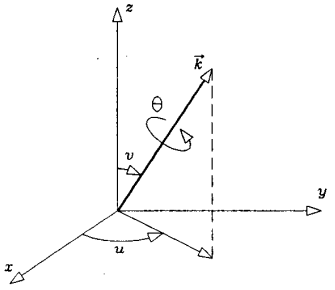

Fig. 2. Equivalent representations of the rotation operator.

II. EQUIVALENT REPRESENTATIONS OF HOMOGENEOUS TRANSFORM

The homogeneous transform that describes the relative position and orientation of a frame with reference to the other one has six degrees of freedom: three for the 3-D position and the other three for the 3-D orientation. It has the following 4×4 matrix representation of T [25].

$$T = \left[\begin{array}{c|c} R & \vec{p} \\ \hline 000 & 1 \end{array}\right]$$

where $R = (\vec{r}_1, \vec{r}_2, \vec{r}_3) = [r_{ij}]$ is the 3×3 rotation matrix, and $\vec{p} = (x, y, z)^t$ is the translation vector; the superscript t denotes transpose.

As shown in Fig. 2, the rotation can be represented by three independent parameters: two angles, u and v, to define the axis of rotation $\vec{k}$, and an angle θ to specify the amount of rotation. Let $\vec{t} = (u, v, \theta, x, y, z)^t$. Matrix T and vector $\vec{t}$ are equivalent representations of the homogeneous transform. Define $\vec{r} = (u, v, \theta)^t$. Matrix R, vector $\vec{r}$ and operator $\mathrm{Rot}(\vec{k}, \theta)$ are equivalent representations of the rotation operation, where $\vec{k} = (\sin v \cdot \cos u, \sin v \cdot \sin u, \cos v)^t$ is the generalized axis of rotation. Equivalent representations will be used alternatively depending on the appropriateness.

III. CLASS A CALIBRATION PROCEDURE

Let the $\{0\}$-frame be the world coordinate system attached to the manipulator base and the $\{\phi\}$-frame be the body frame of the fixed reference object. Fig. 3 depicts frames of the transformation chain used in the extrinsic calibration, where the $\{n|\vec{q}\}$-frame and the$\{s|\vec{q}\}$-frame denote, respectively, the $\{n\}$-frame and the $\{s\}$-frame as the manipulator holds at joint

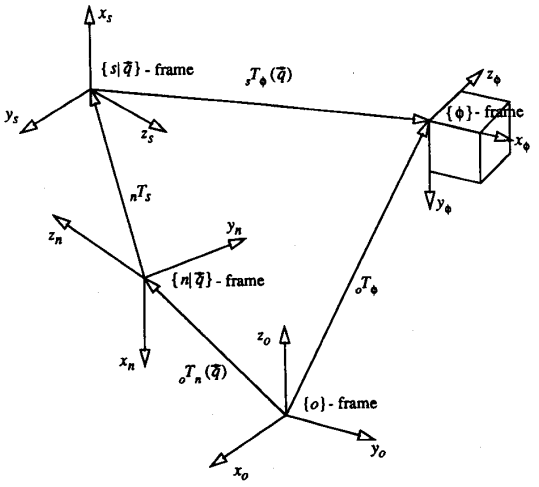

Fig. 3. The transformation chain of manipulator, sensor, and reference object.

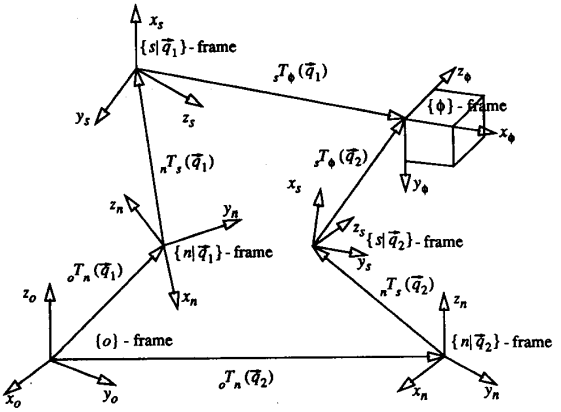

Fig. 4. Transformation chains at $\vec{q}_1$ and $\vec{q}_2$.

angles $\vec{q}$. Transformation arithmetic yields

$${}_nT_s = {}_0T_n^{-1}(\vec{q})\ {}_0T_\phi\ {}_sT_\phi^{-1}(\vec{q}) \tag{1}$$

where ${}_\alpha T_\beta$ is the transformation matrix describing the $\{\beta\}$-frame in the $\{\alpha\}$-frame, and ${}_\alpha T_\beta(\vec{q})$ describes the $\{\beta\}$-frame in the $\{\alpha\}$-frame when the manipulator holds at $\vec{q}$. ${}_0T_n(\vec{q})$ is computed using the forward kinematics of the host manipulator. The vision sensor makes ${}_sT_\phi(\vec{q})$ available [33], [37]. The sensor's mounting position, ${}_nT_s$ as described in the $\{n\}$-frame, can be easily identified using (1) if ${}_0T_\phi$ is known.

IV. CLASS B CALIBRATION PROCEDURE

Pause the manipulator at $\vec{q}_1$ and $\vec{q}_2$, as shown in Fig. 4, where the sensor gathers ${}_sT_\phi(\vec{q}_1)$ and ${}_sT_\phi(\vec{q}_2)$. The transformation arithmetic yields

$${}_{n_1}T_{n_2}\ {}_nT_s = {}_nT_s\ {}_{s_1}T_{s_2} \tag{2}$$

where ${}_{n_i}T_{n_j} = {}_0T_n^{-1}(\vec{q}_i)\ {}_0T_n(\vec{q}_j)$, and ${}_{s_i}T_{s_j} = {}_sT_\phi(\vec{q}_i)\ {}_sT_\phi^{-1}(\vec{q}_j)$.

Let $\mathcal{X}$ and $\vec{x} = (x, y, z)^t$ be the respective rotation matrix and translation vector of the to-be-calibrated ${}_nT_s$. Equation (2) appears as follows:

$$ {}_{n_1}R_{n_2}\,\mathcal{X} = \mathcal{X}\,{}_{s_1}R_{s_2} \tag{3} $$

$$ ({}_{n_1}R_{n_2} - I_{3\times 3})\,\vec{x} = \mathcal{X}\,{}_{s_1}\vec{p}_{s_2} - {}_{n_1}\vec{p}_{n_2} \tag{4} $$

where $I_{3\times 3}$ is the 3×3 identity matrix, and ${}_{\alpha_i}R_{\alpha_j}$ and ${}_{\alpha_i}\vec{p}_{\alpha_j}$ are the respective 3×3 rotation matrix and 3×1 translation vector of ${}_{\alpha_i}T_{\alpha_j}$.

It is noted that ${}_0R_n(\vec{q}_1) = {}_0R_n(\vec{q}_2)$, i.e., link n remains in the same orientation at both $\vec{q}_1$ and $\vec{q}_2$, results in ${}_{n_1}R_{n_2} = {}_{s_1}R_{s_2} = I_{3\times 3}$. In turn, (3) becomes the null equality, i.e., $0 = 0$, which offers no information for identifying $\mathcal{X}$. Such an undesirable condition should be avoided.

Since $\vec{x}$ does not appear in (3) while $\mathcal{X}$ does in (4), (3) and (4) are *decoupled* and $\mathcal{X}$ is resolved before $\vec{x}$. Solving (3) for $\mathcal{X}$ is a *nonlinear* problem, whereas solving (4) for $\vec{x}$ is a *linear* one. In the rest of this section, solutions of $\mathcal{X}$ and $\vec{x}$ are derived in Subsections IV-A and IV-B, respectively. Then, the class B calibration procedure is presented in Subsection IV-C and followed by the error analysis in Subsection IV-D.

A. Closed-Form Solutions of the Rotation Matrix $\mathcal{X}$

The sensor is fixed to the mounted link n. When link n moves, its rotation is the same as that of the sensor. The ${}_{n_1}R_{n_2}$ operator, as described in the $\{n|\vec{q}_1\}$-frame, turns the orientation of the $\{n|\vec{q}_2\}$-frame into that of the $\{n|\vec{q}_1\}$-frame. Simultaneously, the ${}_{s_1}R_{s_2}$ operator, as described in the $\{s|\vec{q}_1\}$-frame, rotates the orientation of the $\{s|\vec{q}_2\}$-frame into that of the $\{s|\vec{q}_1\}$-frame. ${}_{n_1}R_{n_2}$ and ${}_{s_1}R_{s_2}$ represent the same rotation operation in the $\{n|\vec{q}_1\}$-frame and the $\{s|\vec{q}_1\}$-frame, respectively. The following theorems, proved in Appendix IV, pave the way for resolving $\mathcal{X}$ of (3).

Theorem 1: Let ${}_{n_1}R_{n_2} = \mathrm{Rot}({}_{n_1}\vec{k}_{n_2}, {}_{n_1}\theta_{n_2})$ and ${}_{s_1}R_{s_2} = \mathrm{Rot}({}_{s_1}\vec{k}_{s_2}, {}_{s_1}\theta_{s_2})$. Then ${}_{n_1}\vec{k}_{n_2}$ and ${}_{s_1}\vec{k}_{s_2}$ represent the same vector in the $\{n|\vec{q}_1\}$-frame and the $\{s|\vec{q}_1\}$-frame. Furthermore, ${}_{n_1}\theta_{n_2} = {}_{s_1}\theta_{s_2}$.

${}_{n_1}\vec{k}_{n_2}$ and ${}_{s_1}\vec{k}_{s_2}$ represent the same vector in the $\{n|\vec{q}_1\}$-frame and the $\{s|\vec{q}_1\}$-frame, whose relative orientation as described in the $\{n|\vec{q}_1\}$-frame is $\mathcal{X}$. Therefore, $\mathcal{X}$ is characterized by the rotation operator that maps ${}_{s_1}\vec{k}_{s_2}$ onto ${}_{n_1}\vec{k}_{n_2}$, i.e., $\mathcal{X}\ {}_{s_1}\vec{k}_{s_2} = {}_{n_1}\vec{k}_{n_2}$, as stated in the following theorem.

Theorem 2: ${}_{n_1}R_{n_2}\,\mathcal{X} = \mathcal{X}\,{}_{s_1}R_{s_2}$ if and only if $\mathcal{X}\ {}_{s_1}\vec{k}_{s_2} = {}_{n_1}\vec{k}_{n_2}$.

Theorem 2 discloses that $\mathcal{X}$ cannot be the identity matrix $I_{3\times 3}$ unless ${}_{n_1}\vec{k}_{n_2} = {}_{s_1}\vec{k}_{s_2}$. However, when ${}_{n_1}\vec{k}_{n_2} = {}_{s_1}\vec{k}_{s_2}$, both $\mathcal{X} \neq I_{3\times 3}$ and $\mathcal{X} = I_{3\times 3}$ are possible. They constitute special cases and the following corollary deserves attention.

Corollary 2.1: Let ${}_{n_1}\vec{k}_{n_2} = {}_{s_1}\vec{k}_{s_2}$. Denote $\mathrm{Rot}(\vec{k}_\mathcal{X}, \theta_\mathcal{X})$ as the operator representation of $\mathcal{X}$. Then ${}_{n_1}R_{n_2}\,\mathcal{X} = \mathcal{X}\,{}_{s_1}R_{s_2}$ if and only if $\vec{k}_\mathcal{X} = {}_{n_1}\vec{k}_{n_2} = {}_{s_1}\vec{k}_{s_2}$ and $\mathcal{X} \in \{\mathrm{Rot}(\vec{k}_\mathcal{X}, \theta)|0 < \theta < 2\pi\} \cup \{\mathrm{Rot}(\vec{k}, \theta_\mathcal{X})|\,\|\vec{k}\| = 1, \theta_\mathcal{X} = 0\}$. Furthermore, $\mathcal{X} \in \{\mathrm{Rot}(\vec{k}_\mathcal{X}, \theta)|0 < \theta < 2\pi\}$ when $\mathcal{X} \neq I_{3\times 3}$, and $\mathcal{X} \in \{\mathrm{Rot}(\vec{k}, \theta_\mathcal{X})|\,\|\vec{k}\| = 1, \theta_\mathcal{X} = 0\}$ when $\mathcal{X} = I_{3\times 3}$.

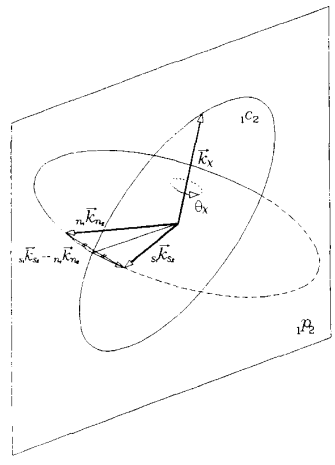

Fig. 5. $\vec{k}_\mathcal{X} \in {}_1C_2$ where $\mathrm{Rot}(\vec{k}_\mathcal{X}, \theta_\mathcal{X})\,{}_{s_1}\vec{k}_{s_2} = {}_{n_1}\vec{k}_{n_2}$.

Theorem 2 has shown that every rotation matrix $\mathcal{X}$ having $\mathcal{X}\ {}_{s_1}\vec{k}_{s_2} = {}_{n_1}\vec{k}_{n_2}$ is a solution of (3). When ${}_{n_1}\vec{k}_{n_2} \neq {}_{s_1}\vec{k}_{s_2}$, the vector analysis reveals that $\vec{k}_\mathcal{X}$, as shown in Fig. 5, lies on the ${}_1P_2$ plane, which contains the origin and is the perpendicular bisection plane of $({}_{s_1}\vec{k}_{s_2} - {}_{n_1}\vec{k}_{n_2})$. $\vec{k}_\mathcal{X}$ is of unit length. Its tail end sits at the origin, and the head end lies on the unit circle ${}_1C_2$ where the unit sphere intersects ${}_1P_2$. Every unit vector $\vec{k}_\mathcal{X}$ having the head end on ${}_1C_2$ is the generalized rotation axis of a rotation operator that solves (3). It is noted that the head ends of ${}_{n_1}\vec{k}_{n_2}$ and ${}_{s_1}\vec{k}_{s_2}$ are at the same latitude of the unit spinning sphere whose axis of rotation is $\vec{k}_\mathcal{X}$. When ${}_{n_1}\vec{k}_{n_2} = {}_{s_1}\vec{k}_{s_2}$ occurs, $\vec{k}_\mathcal{X} = {}_{n_1}\vec{k}_{n_2} = {}_{s_1}\vec{k}_{s_2}$ as stated in Corollary 2.1. However, the rotation angle $\theta_\mathcal{X}$ remains unknown. Therefore, (3) is an *underdetermined nonlinear* system. To resolve $\mathcal{X}$, the manipulator has to be displaced at least twice.

Define $I_\alpha = \{1, 2, \ldots, \alpha\}$ as the integer index set of 1 to α. Collect ${}_0T_n(\vec{q}_\gamma)$ and ${}_sT_\phi(\vec{q}_\gamma)$, where $\gamma \in I_{m+2}$ and $m \geq 1$. It is shown in Appendix I that three samples obtained at $\vec{q}_i$, $\vec{q}_j$ and $\vec{q}_k$ resolve $\mathcal{X}$. The solutions, indexed by i, are summarized below.

Case 1.1: If ${}_{n_i}\vec{k}_{n_j} \neq {}_{s_i}\vec{k}_{s_j}$, ${}_{n_i}\vec{k}_{n_k} \neq {}_{s_i}\vec{k}_{s_k}$ and $\|({}_{n_i}\vec{k}_{n_j} - {}_{s_i}\vec{k}_{s_j}) \times ({}_{n_i}\vec{k}_{n_k} - {}_{s_i}\vec{k}_{s_k})\| \neq 0$, then

$$ \vec{k}_{\mathcal{X}_i} = \frac{({}_{n_i}\vec{k}_{n_j} - {}_{s_i}\vec{k}_{s_j}) \times ({}_{n_i}\vec{k}_{n_k} - {}_{s_i}\vec{k}_{s_k})}{\|({}_{n_i}\vec{k}_{n_j} - {}_{s_i}\vec{k}_{s_j}) \times ({}_{n_i}\vec{k}_{n_k} - {}_{s_i}\vec{k}_{s_k})\|} \tag{5} $$

$$ \theta_{\mathcal{X}_i} = \sum_{\varrho\in\{j,k\}} \mathrm{sgn}(\zeta_\varrho^i)\,\tan^{-1}\left(\frac{\|{}_{n_i}\vec{k}_{n_\varrho} - {}_{s_i}\vec{k}_{s_\varrho}\|}{\|\vec{k}_{\mathcal{X}_i} \times ({}_{n_i}\vec{k}_{n_\varrho} + {}_{s_i}\vec{k}_{s_\varrho})\|}\right) \tag{6} $$

where $\zeta_\varrho^i = ({}_{n_i}\vec{k}_{n_\varrho} - {}_{s_i}\vec{k}_{s_\varrho})^t\left(\vec{k}_{\mathcal{X}_i} \times ({}_{n_i}\vec{k}_{n_\varrho} + {}_{s_i}\vec{k}_{s_\varrho})\right)$.

Case 1.2: If ${}_{n_i}\vec{k}_{n_j} \neq {}_{s_i}\vec{k}_{s_j}$, ${}_{n_i}\vec{k}_{n_k} \neq {}_{s_i}\vec{k}_{s_k}$ and $\|({}_{n_i}\vec{k}_{n_j} - {}_{s_i}\vec{k}_{s_j}) \times ({}_{n_i}\vec{k}_{n_k} - {}_{s_i}\vec{k}_{s_k})\| = 0$, then

$$ \vec{k}_{\mathcal{X}_i} = -({}_{n_i}\vec{k}_{n_j} \times {}_{n_i}\vec{k}_{n_k}) \times ({}_{s_i}\vec{k}_{s_j} \times {}_{s_i}\vec{k}_{s_k}) \tag{7} $$

$$ \theta_{\mathcal{X}_i} = \cos^{-1}\left(({}_{n_i}\vec{k}_{n_j} \times {}_{n_i}\vec{k}_{n_k})^t({}_{s_i}\vec{k}_{s_j} \times {}_{s_i}\vec{k}_{s_k})\right). \tag{8} $$

Case 2: If ${}_{n_i}\vec{k}_{n_j} = {}_{s_i}\vec{k}_{s_j}$ and ${}_{n_i}\vec{k}_{n_k} \neq {}_{s_i}\vec{k}_{s_k}$, then

$$\vec{k}_{\mathcal{X}_i} = {}_{n_i}\vec{k}_{n_j} = {}_{s_i}\vec{k}_{s_j}$$

$$\theta_{\mathcal{X}_i} = 2\,\mathrm{sgn}(\zeta_k^i)\tan^{-1}\left(\frac{\|{}_{n_i}\vec{k}_{n_k} - {}_{s_i}\vec{k}_{s_k}\|}{\|\vec{k}_{\mathcal{X}_i} \times ({}_{n_i}\vec{k}_{n_k} + {}_{s_i}\vec{k}_{s_k})\|}\right). \quad (9)$$

Case 3: If ${}_{n_i}\vec{k}_{n_j} \neq {}_{s_i}\vec{k}_{s_j}$ and ${}_{n_i}\vec{k}_{n_k} = {}_{s_i}\vec{k}_{s_k}$, then

$$\vec{k}_{\mathcal{X}_i} = {}_{n_i}\vec{k}_{n_k} = {}_{s_i}\vec{k}_{s_k}$$

$$\theta_{\mathcal{X}_i} = 2\,\mathrm{sgn}(\zeta_j^i)\tan^{-1}\left(\frac{\|{}_{n_i}\vec{k}_{n_j} - {}_{s_i}\vec{k}_{s_j}\|}{\|\vec{k}_{\mathcal{X}_i} \times ({}_{n_i}\vec{k}_{n_j} + {}_{s_i}\vec{k}_{s_j})\|}\right). \quad (10)$$

Case 4: If ${}_{n_i}\vec{k}_{n_j} = {}_{s_i}\vec{k}_{s_j}$ and ${}_{n_i}\vec{k}_{n_k} = {}_{s_i}\vec{k}_{s_k}$, then

$$\mathrm{Rot}(\vec{k}_{\mathcal{X}_i}, \theta_{\mathcal{X}_i}) = I_{3\times 3}. \quad (11)$$

B. Closed-Form Solution of the Translation Vector $\vec{x}$

This subsection proceeds to resolve $\vec{x}$. Equation (4) is linear. At a glance, premultiplying the inverse of $({}_{n_1}R_{n_2} - I_{3\times 3})$ to both sides of (4) should have resolved $\vec{x}$ immediately. Unfortunately, $({}_{n_1}R_{n_2} - I_{3\times 3})$ is rank deficient. No inverse exists. Equation (4), like (3), is *underdetermined*. Therefore, not only for the identification of $\mathcal{X}$ but also for $\vec{x}$, observations of ${}_0T_n(\vec{q})$ and ${}_sT_\phi(\vec{q})$ have to be gathered at no less than three manipulator configurations. This subsection presents the solution of $\vec{x}$ first. Then the undesirable experimental condition is briefly addressed.

Collect samples at $\vec{q}_1$, $\vec{q}_2$, and $\vec{q}_3$. Define $R_B[\vec{q}|3]$ and $\vec{p}_B[\vec{q}|3]$ as follows:

$$R_B[\vec{q}|3] = \begin{bmatrix} {}_{n_1}R_{n_2} - I_{3\times 3} \\ {}_{n_2}R_{n_3} - I_{3\times 3} \end{bmatrix}$$

$$\vec{p}_B[\vec{q}|3] = \begin{bmatrix} \mathcal{X}\,{}_{s_1}\vec{p}_{s_2} - {}_{n_1}\vec{p}_{n_2} \\ \mathcal{X}\,{}_{s_2}\vec{p}_{s_3} - {}_{n_2}\vec{p}_{n_3} \end{bmatrix}.$$

The following theorem resolves $\vec{x}$.

Theorem 3: $R_B[\vec{q}|3]$ is of full rank if and only if ${}_{n_1}\vec{k}_{n_2} \neq \pm\,{}_{n_2}\vec{k}_{n_3}$. In addition,

$$\vec{x} = \left(R_B[\vec{q}|3]^t R_B[\vec{q}|3]\right)^{-1} R_B[\vec{q}|3]^t\, \vec{p}_B[\vec{q}|3]. \quad (12)$$

The determinant of $(R_B[\vec{q}|3]^t R_B[\vec{q}|3])$, by direct evaluation, is nontrivial if and only if ${}_{n_1}\vec{k}_{n_2}$ and ${}_{n_2}\vec{k}_{n_3}$ are neither parallel nor antiparallel. The direct evaluation plainly proves Theorem 3. It offers no insight about the undesirable experimental condition. The following illustration sheds light on why ${}_{n_1}\vec{k}_{n_2} = \pm\,{}_{n_2}\vec{k}_{n_3}$ constitutes the undesirable experimental condition.

Assign $\vec{z}_{\{n|\vec{q}_1\}}$, the z-axis of the $\{n|\vec{q}_1\}$-frame, to be parallel with ${}_{n_1}\vec{k}_{n_2}$ without loss of generality. Then $\vec{z}_{\{n|\vec{q}_2\}}$ is also parallel with ${}_{n_1}\vec{k}_{n_2}$ and ${}_{n_1}R_{n_2} = \mathrm{Rot}(\vec{z}_{\{n|\vec{q}_1\}}, {}_{n_1}\theta_{n_2})$. Equation (4), described in the $\{n|\vec{q}_1\}$-frame, appears as follows:

$$\begin{bmatrix} \cos({}_{n_1}\theta_{n_2}) - 1 & -\sin({}_{n_1}\theta_{n_2}) & 0 \\ \sin({}_{n_1}\theta_{n_2}) & \cos({}_{n_1}\theta_{n_2}) - 1 & 0 \\ 0 & 0 & 0 \end{bmatrix} \vec{x} = \mathcal{X}\,{}_{s_1}\vec{p}_{s_2} - {}_{n_1}\vec{p}_{n_2}. \quad (13)$$

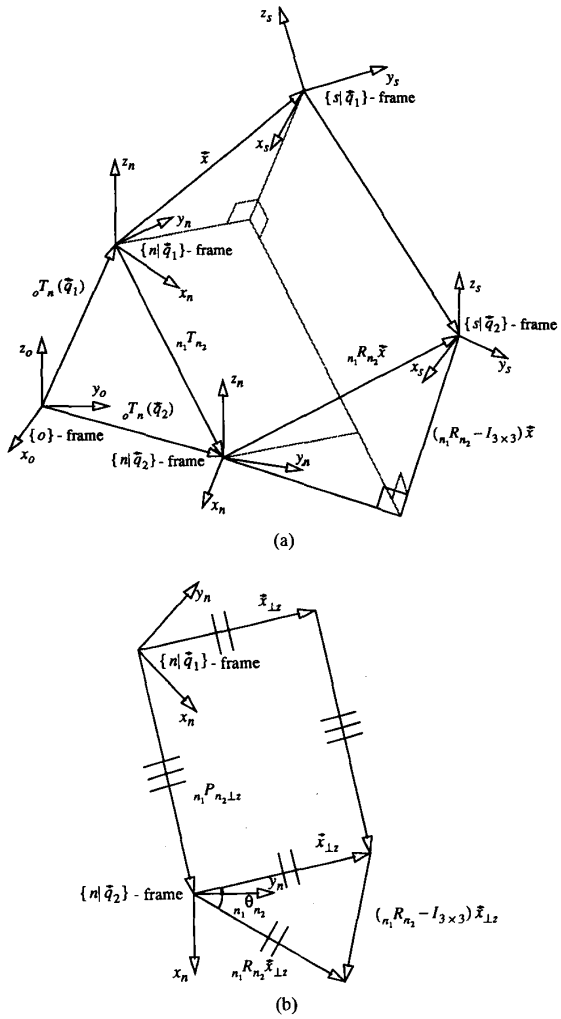

Fig. 6. (a) Transformation chains described by (13). (b) The orthographic projection of transformation chains on the x_n–y_n plane. $\vec{x}_{\perp z} = (x, y, 0)^t$ is the orthographic projection of $\vec{x}$ on the x_n–y_n plane. ${}_{n_1}P_{n_2\perp z}$ is the orthographic projection of ${}_{n_1}\vec{P}_{n_2}$ on the x_n–y_n plane.

The first two equations resolve x and y unless ${}_{n_1}\theta_{n_2} = 0$, an undesirable condition that should have been avoided. The third equation is a null equality. Equation (13) contains no information for resolving z, which, from a more systematic point of view, represents the orthographic projection of $\vec{x}$ on the generalized rotation axis ${}_{n_1}\vec{k}_{n_2}$. Fig. 6(a) sketches the 3-D relationship described by (13). Fig. 6(b), the orthographic projection of Fig. 6(a) on the x–y plane, shows the 2-D relationship of (13) on the x–y plane of the $\{n|\vec{q}_1\}$-frame.

The above discussions show that every time link n is displaced by a nontrivial amount of rotation, (13) recovers components of $\vec{x}$ perpendicular to the axis of rotation. Therefore, $R_B[\vec{q}|3]$ is of full rank and (12) resolves $\vec{x}$ whenever ${}_{n_1}\vec{k}_{n_2} \neq \pm\,{}_{n_2}\vec{k}_{n_3}$.

C. Steps of the Class B Calibration Procedure

Solutions presented in the last subsection cannot miss the

true $\mathcal{X}$ and $\vec{x}$ if error-free samples are used. Unfortunately, measurement errors exist causing calibration inaccuracies [35], [36]. To improve the calibration accuracy, samples of ${}_0T_n(\vec{q}_i)$ and ${}_sT_\phi(\vec{q}_i)$, $i \in I_{m+2}$, $m \geq 1$ are collected. Steps for the class B calibration procedure follow.

Step 1: Let $j = i+1$ and $k = j+1$. Calculate $\text{Rot}(\vec{k}_{\mathcal{X}_i}, \theta_{\mathcal{X}_i})$ for $i \in I_m$ using (5)–(11).

Step 2: Let $\vec{r}_{\mathcal{X}_i}$ be the vector representation of $\text{Rot}(\vec{k}_{\mathcal{X}_i}, \theta_{\mathcal{X}_i})$. Compute $\hat{r}$ and $\text{Cov}(\hat{r})$ as

$$\hat{r} = \sum_{i=1}^{m} \frac{\vec{r}_{\mathcal{X}_i}}{m} \tag{14}$$

$$\text{Cov}(\hat{r}) = \sum_{i=1}^{m} \frac{(\vec{r}_{\mathcal{X}_i} - \hat{r})(\vec{r}_{\mathcal{X}_i} - \hat{r})^t}{m \cdot (m-1)}. \tag{15}$$

Step 3: Let $\hat{\mathcal{X}}$ be the matrix representation of $\hat{r}$ obtained at Step 2. Construct

$$R_B[\vec{q}|m+2] = \begin{bmatrix} {}_{n_1}R_{n_2} - I_{3\times 3} \\ \vdots \\ {}_{n_{m+1}}R_{n_{m+2}} - I_{3\times 3} \end{bmatrix}$$

$$\vec{p}_B[\vec{q}|m+2] = \begin{bmatrix} \hat{\mathcal{X}}\,{}_{s_1}\vec{p}_{s_2} - {}_{n_1}\vec{p}_{n_2} \\ \vdots \\ \hat{\mathcal{X}}\,{}_{s_{m+1}}\vec{p}_{s_{m+2}} - {}_{n_{m+1}}\vec{p}_{n_{m+2}} \end{bmatrix}.$$

Step 4: Compute $\hat{x}$ and $\text{Cov}(\hat{x})$ using

$$\hat{x} = (R_B[\vec{q}|m+2]^t R_B[\vec{q}|m+2])^{-1} \cdot R_B[\vec{q}|m+2]^t \vec{p}_B[\vec{q}|m+2] \tag{16}$$

$$\text{Cov}(\hat{x}) = (R_B[\vec{q}|m+2]^t R_B[\vec{q}|m+2])^{-1} \cdot \hat{\sigma}^2 \tag{17}$$

$$\hat{\sigma}^2 = \frac{\|\vec{p}_B[\vec{q}|m+2] - R_B[\vec{q}|m+2]\hat{x}\|^2}{3 \cdot (m+1)}. \tag{18}$$

$\hat{r}$ and $\hat{x}$, whose accuracies are assessed by $\text{Cov}(\hat{r})$ and $\text{Cov}(\hat{x})$ respectively, identify $\mathcal{X}$ and $\vec{x}$.

D. Error Analysis

Measurement uncertainties introduce calibration inaccuracies whose magnitudes depend on the experimental conditions. In this subsection, the relationship between magnitudes of random errors and calibration inaccuracies is examined. Thereby, unstable calibrations can be avoided.

1) Stable and Unstable Calibration Conditions for $\mathcal{X}$: Conditions making the calibration of $\vec{k}_{\mathcal{X}}$ and $\theta_{\mathcal{X}}$ sensitive and insensitive to random errors are presented in Appendix II. One of the unstable conditions is $\theta_{\mathcal{X}} = 0$, whereas $|\theta_{\mathcal{X}}| = \pi/2$ constitutes a part of the most stable condition. In the case where perfect alignment between the vision sensor and the mounted link is desirable, $\theta_{\mathcal{X}} \simeq 0$ and an unstable calibration condition is forged. A remedy follows. Let the $\{n'\}$-frame, an auxiliary frame fixed to both the $\{n\}$- and $\{s\}$-frames, be $\pi/2$ out of phase with the $\{n\}$-frame, i.e., ${}_nR_{n'} = \text{Rot}({}_n\vec{k}_{n'}, \pm\pi/2)$, where ${}_n\vec{k}_{n'}$ is an arbitrarily selected axis of rotation. Then, instead of identifying $\mathcal{X}$, i.e., ${}_nR_s$, calibrate $\mathcal{X}'$, i.e., ${}_{n'}R_s$. Once $\mathcal{X}'$ is resolved, $\mathcal{X} = {}_nR_{n'}\mathcal{X}'$ is obtained. In general, the desirable calibration condition of $|\theta_{\mathcal{X}}| \simeq \pi/2$ can always be set by introducing the auxiliary $\{n'\}$-frame of ${}_nR_{n'} = \hat{\mathcal{X}}\,\text{Rot}(\vec{k}, \pm\pi/2)$, where $\vec{k}$ is arbitrarily chosen and $\hat{\mathcal{X}}$ is the prior estimate of $\mathcal{X}$.

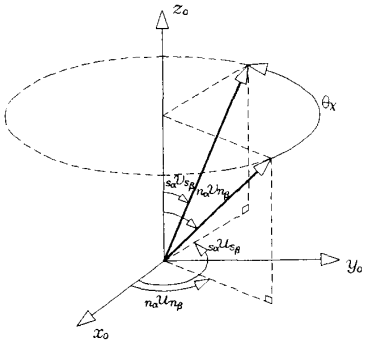

Fig. 7. $({}_{n_\alpha}u_{n_\beta}, {}_{n_\alpha}v_{n_\beta})$ and $({}_{s_\alpha}u_{s_\beta}, {}_{s_\alpha}v_{s_\beta})$ define ${}_{n_\alpha}\vec{k}_{n_\beta}$ and ${}_{s_\alpha}\vec{k}_{s_\beta}$ in the $\{o\}$-frame where ${}_{s_\alpha}u_{s_\beta} = {}_{n_\alpha}u_{n_\beta} + \theta_{\mathcal{X}}$ and ${}_{s_\alpha}v_{s_\beta} = {}_{n_\alpha}v_{n_\beta}$.

Let the observer $\{o\}$-frame be characterized by ${}_nR_o\vec{k}_{\mathcal{X}} = (0,\ 0,\ 1)^t$, in which $\mathcal{X}$ appears to be $\text{Rot}(\vec{z}_o, \theta_{\mathcal{X}})$. In addition, let $({}_{n_\alpha}u_{n_\beta}, {}_{n_\alpha}v_{n_\beta})$ and $({}_{s_\alpha}u_{s_\beta}, {}_{s_\alpha}v_{s_\beta})$ define ${}_{n_\alpha}\vec{k}_{n_\beta}$ and ${}_{s_\alpha}\vec{k}_{s_\beta}$ in the $\{o\}$-frame as shown in Fig. 7. Then $|{}_{n_i}u_{n_k} - {}_{n_i}u_{n_j}| = \pi/2$, $|{}_{n_i}v_{n_\varrho}| = \pi/2$ for $\varrho \in \{j,k\}$ and $|\theta_{\mathcal{X}}| = \pi/2$ constitute the most stable calibration condition as shown in Appendix II. Geometrically, $|{}_{n_i}u_{n_k} - {}_{n_i}u_{n_j}| = \pi/2$ and $|{}_{n_i}v_{n_\varrho}| = \pi/2$, $\varrho \in \{j,k\}$ means that both ${}_{n_i}\vec{k}_{n_j}$ and ${}_{n_i}\vec{k}_{n_k}$ are on the equator of a spinning sphere whose axis is $\vec{k}_{\mathcal{X}}$ and they are separated by an angle of $\pi/2$. Ideally, a sampling plan that collects data around the most stable condition can be designed by using the prior estimate of $\mathcal{X}$. Unfortunately, the settings of $(|{}_{n_i}u_{n_k} - {}_{n_i}u_{n_j}|, {}_{n_i}v_{n_j}, {}_{n_i}v_{n_k}) \simeq (\pi/2, \pi/2, \pi/2)$ may not always be possible because of physical restrictions although $|\theta_{\mathcal{X}}| \simeq \pi/2$ can always be set by introducing the auxiliary frame.

To assess the magnitude of the calibration inaccuracy, the measurement of $\mathcal{N}(\hat{\mathcal{X}}, \mathcal{X})$ as introduced in Appendix III is calculated for various experimental conditions of $\theta_{\mathcal{X}} = \pi/2$. Let the perturbed ${}_{n_\alpha}u_{n_\beta}$, ${}_{s_\alpha}u_{s_\beta}$, ${}_{n_\alpha}v_{n_\beta}$ and ${}_{s_\alpha}v_{s_\beta}$ be within the $\pm\epsilon$ ranges of the true values, where ϵ denotes the magnitude of random errors. The largest $\mathcal{N}(\hat{\mathcal{X}}, \mathcal{X})$, i.e., the most inaccurate result could be caused by random errors, is searched and plotted against ϵ in Fig. 8 for several informative settings, where ϵ increases from 0° to 15°. It has been observed that the calibration inaccuracies under $(|{}_{n_i}u_{n_k} - {}_{n_i}u_{n_j}|, {}_{n_i}v_{n_j}, {}_{n_i}v_{n_k}) = (\pi/2, \pi/2, \pi/2)$ are consistently the smallest.

2) Unstable and Stable Calibration Conditions for $\vec{x}$: Equations (16) and (17) disclose that the calibration of $\vec{x}$ is sensitive to random errors when the true $R_B[\vec{q}|m+2]$ matrix is collinear (or rank deficient). Theorem 3 shows that collinearity does not take place unless ${}_{n_i}\vec{k}_{n_{i+1}} = \pm\,{}_{n_{i+1}}\vec{k}_{n_{i+2}}$ for all $i \in I_{m+1}$, i.e., all of them are either parallel or antiparallel to each other.

The most stable calibration condition takes place when $|{}_{n_i}\theta_{n_{i+1}}| = \pi$ for $i \in I_{m+1}$ and ${}_{n_i}\vec{k}_{n_{i+1}}$, ${}_{n_{i+1}}\vec{k}_{n_{i+2}}$ and ${}_{n_{i+2}}\vec{k}_{n_{i+3}}$ are mutually perpendicular to each other for $i = 1, 4, \ldots$ and $m-1$, where $\text{mod}(m+2, 3) = 1$ and $m \geq 2$

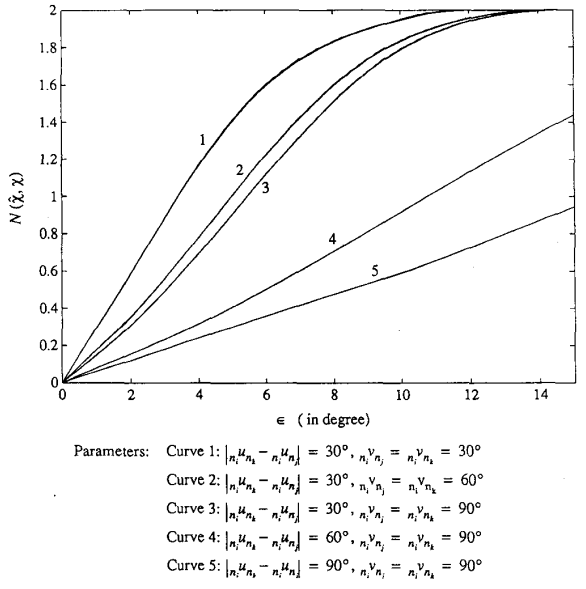

Fig. 8. Magnitudes of calibration inaccuracies.

are assumed. The following equation, derived from (13), demonstrates how ${}_{n_1}\theta_{n_2}$ determines the sensitivity of x and y to random errors.

$$\begin{bmatrix} x \\ y \end{bmatrix} = \frac{1}{(1-\cos({}_{n_1}\theta_{n_2}))^2} \begin{bmatrix} 1 & 0 & 0 \\ 0 & 1 & 0 \end{bmatrix} (\mathcal{X}\, {}_{s_1}\vec{p}_{s_2} - {}_{n_1}\vec{p}_{n_2}). \tag{19}$$

When $|{}_{n_1}\theta_{n_2}|$ approaches 0, x and y are sensitive to random errors. They are most stable when $|{}_{n_1}\theta_{n_2}| = \pi$. Keep ${}_{n_i}\theta_{n_{i+1}} = \pi$, $i \in I_{m+1}$ and let every three ${}_{n_i}\vec{k}_{n_{i+1}}$, ${}_{n_{i+1}}\vec{k}_{n_{i+2}}$ and ${}_{n_{i+2}}\vec{k}_{n_{i+3}}$ mutually orthogonal to each other for $i = 1, 4, \ldots$ and $m-1$. Then $R_B[\vec{q}|m+2]^t R_B[\vec{q}|m+2] = (8 \cdot (m+1)/3)\, I_{3\times 3}$ and every component of $\vec{x}$ is equally insensitive to random errors as asserted by (17).

V. Class C Calibration Procedure

The class C calibration procedure, by taking advantage of the dexterous manipulator, requires no reference object but the simplest one—a fixed point. Instead of using a well-structured reference object, it adopts structured manipulator configurations while sampling. This section presents the class C calibration procedure. The orientation matrix $\mathcal{X}$ and the translation vector $\vec{x}$ are resolved in Subsections V-A and V-B, respectively. Then Subsection V-C presents steps of the class C calibration procedure.

A. Closed-Form Solutions of $\mathcal{X}$

A fixed point $\mathcal{P}$ lies within the sensing range. Let its coordinates be ${}_0\vec{p}_\phi$ in the $\{0\}$-frame and ${}_s\vec{p}_\phi(\vec{q})$ in the $\{s|\vec{q}\}$-frame. The transformation arithmetic yields

$${}_0\vec{p}_\phi = {}_0R_n(\vec{q})(\mathcal{X}\, {}_s\vec{p}_\phi(\vec{q}) + \vec{x}) + {}_0\vec{p}_n(\vec{q}). \tag{20}$$

Take samples of ${}_0R_n^{-1}(\vec{q}_i)$, ${}_0\vec{p}_n(\vec{q}_i)$ and ${}_s\vec{p}_\phi(\vec{q}_i)$ for $i = 1$ and 2, where ${}_0R_n(\vec{q}_1) = {}_0R_n(\vec{q}_2)$. Equation (20) yields

$$\mathcal{X}\,({}_s\vec{p}_\phi(\vec{q}_1) - {}_s\vec{p}_\phi(\vec{q}_2)) = {}_0R_n^{-1}(\vec{q}_i)({}_0\vec{p}_n(\vec{q}_2) - {}_0\vec{p}_n(\vec{q}_1)), \quad i = \text{either 1 or 2.} \tag{21}$$

$\mathcal{X}$, as characterized by (21), maps $({}_s\vec{p}_\phi(\vec{q}_1) - {}_s\vec{p}_\phi(\vec{q}_2))$ onto ${}_0R_n^{-1}(\vec{q}_i)({}_0\vec{p}_n(\vec{q}_2) - {}_0\vec{p}_n(\vec{q}_1))$. Equation (21) is *underdetermined*. It takes at least two sets of such equations to resolve $\mathcal{X}$. Keep the orientation of link n unchanged while taking one more sample at $\vec{q}_3$. Then assign ${}_{n_1}\vec{k}_{n_2}$, ${}_{s_1}\vec{k}_{s_2}$, ${}_{n_1}\vec{k}_{n_3}$ and ${}_{s_1}\vec{k}_{s_3}$ as follows:

$${}_{n_1}\vec{k}_{n_2} = {}_0R_n^{-1}(\vec{q}_i)({}_0\vec{p}_n(\vec{q}_2) - {}_0\vec{p}_n(\vec{q}_1))/\|{}_0R_n^{-1}(\vec{q}_i)({}_0\vec{p}_n(\vec{q}_2) - {}_0\vec{p}_n(\vec{q}_1))\| \tag{22}$$

$${}_{s_1}\vec{k}_{s_2} = ({}_s\vec{p}_\phi(\vec{q}_1) - {}_s\vec{p}_\phi(\vec{q}_2))/\|{}_s\vec{p}_\phi(\vec{q}_1) - {}_s\vec{p}_\phi(\vec{q}_2)\| \tag{23}$$

$${}_{n_1}\vec{k}_{n_3} = {}_0R_n^{-1}(\vec{q}_i)({}_0\vec{p}_n(\vec{q}_3) - {}_0\vec{p}_n(\vec{q}_1))/\|{}_0R_n^{-1}(\vec{q}_i)({}_0\vec{p}_n(\vec{q}_3) - {}_0\vec{p}_n(\vec{q}_1))\| \tag{24}$$

$${}_{s_1}\vec{k}_{s_3} = ({}_s\vec{p}_\phi(\vec{q}_1) - {}_s\vec{p}_\phi(\vec{q}_3))/\|{}_s\vec{p}_\phi(\vec{q}_1) - {}_s\vec{p}_\phi(\vec{q}_3)\| \tag{25}$$

where i = either 1, 2, or 3. Applying the solutions presented in Subsection IV-A produces $\text{Rot}(\vec{k}_\mathcal{X}, \theta_\mathcal{X})$.

An undesirable experimental condition occurs whenever ${}_0\vec{p}_n(\vec{q}_1)$, ${}_0\vec{p}_n(\vec{q}_2)$ and ${}_0\vec{p}_n(\vec{q}_3)$ are on a straight line. That condition makes ${}_s\vec{p}_\phi(\vec{q}_1)$, ${}_s\vec{p}_\phi(\vec{q}_2)$ and ${}_s\vec{p}_\phi(\vec{q}_3)$ also lie on a straight line. In turn, it makes ${}_{n_1}\vec{k}_{n_2} = \pm\, {}_{n_1}\vec{k}_{n_3}$ and ${}_{s_1}\vec{k}_{s_2} = \pm\, {}_{s_1}\vec{k}_{s_3}$, the undesirable experimental condition illustrated in Appendix I.

B. Closed-Form Solution of $\vec{x}$

The orientation of link n is kept unchanged while resolving $\mathcal{X}$. It is altered while resolving $\vec{x}$. Hold the manipulator at $\vec{q}_4$ where ${}_0R_n(\vec{q}_4) \neq {}_0R_n(\vec{q}_i)$, $i \in I_3$. Then the following equation is obtained:

$$({}_0R_n(\vec{q}_i) - {}_0R_n(\vec{q}_4))\vec{x} = \vec{p}_R(\vec{q}_4) - \vec{p}_R(\vec{q}_i), \quad \text{for } i = \text{either 1, 2, or 3} \tag{26}$$

where $\vec{p}_R(\vec{q}) = {}_0R_n(\vec{q})\mathcal{X}\, {}_s\vec{p}_\phi(\vec{q}) + {}_0\vec{p}_n(\vec{q})$.

Since $\text{Det}(R_\alpha - R_\beta) = \text{Det}(R_\beta) \cdot \text{Det}\left(R_\beta^{-1}R_\alpha - I_{3\times 3}\right) = 0$ for rotation matrices R_α and R_β, (26) is *underdetermined*. Collect one more sample at $\vec{q}_5$ where, again, the orientation of link n is altered. The undesirable experimental condition, as discussed in Subsection IV-B, occurs when ${}_0R_n^{-1}(\vec{q}_i){}_0R_n(\vec{q}_5)$ and ${}_0R_n^{-1}(\vec{q}_i){}_0R_n(\vec{q}_4)$ share the same axis of rotation. Therefore, in addition to ${}_0R_n(\vec{q}_5) \neq {}_0R_n(\vec{q}_i)$ for $i \in I_4$, let ${}_0R_n^{-1}(\vec{q}_i){}_0R_n(\vec{q}_5)$ and ${}_0R_n^{-1}(\vec{q}_i){}_0R_n(\vec{q}_4)$ share no axis of rotation, i = either 1, 2, or 3. Then the following formula resolves $\vec{x}$:

$$\vec{x} = (R_C[\vec{q}|3]^t R_C[\vec{q}|3])^{-1}\, R_C[\vec{q}|3]^t\, \vec{p}_C[\vec{q}|3] \tag{27}$$

where

$$R_C[\vec{q}|3] = \begin{bmatrix} {}_0R_n(\vec{q}_i) - {}_0R_n(\vec{q}_4) \\ {}_0R_n(\vec{q}_4) - {}_0R_n(\vec{q}_5) \end{bmatrix}$$

$$pCQ3 = \begin{bmatrix} \vec{p}_R(\vec{q}_4) - \vec{p}_R(\vec{q}_i) \\ \vec{p}_R(\vec{q}_5) - \vec{p}_R(\vec{q}_4) \end{bmatrix}$$

for i= either 1, 2, or 3.

C. Steps of the Class C Calibration Procedure

To reduce the calibration inaccuracies caused by experimental errors, a sample size larger than the minimum requirement of 5 is necessary. Let $N(S)$ denote the size of the set S. Let $Q_j = \{\vec{q}_{j,i} | {}_0R_n(\vec{q}_{j,i}) = {}_0R_{n,j}, i \in I_{N(Q_j)}\}$, where $N(Q_j) \geq 1$ and $j \in I_{m+2}$. $Q_1, Q_2, \ldots, Q_{m+2}$ are $m+2$ mutually exclusive sets of manipulator configurations. Every member of Q_j poses the manipulator in the same orientation, i.e., ${}_0R_{n,j}$. Samples of ${}_0R_n(\vec{q})$, ${}_0\vec{p}_n(\vec{q})$ and ${}_s\vec{p}_\phi(\vec{q})$ are collected at $\vec{q} \in \bigcup_{j=1}^{m+2} Q_j$ for the extrinsic calibration, which proceeds as follows.

Step 1: Let $I_R = \{j | j \in I_{m+2}, N(Q_j) \geq 3\}$. Compute $\mathcal{X}_{j,i}$ using (5)–(11), (22)–(25) and samples collected at $\vec{q}_{j,i}$, $\vec{q}_{j,i+1}$, and $\vec{q}_{j,i+2}$, where $j \in I_R$ and $i \in I_{N(Q_j)-2}$.

Step 2: Let $\vec{r}_{j,i}$ be the vector representation of $\mathcal{X}_{j,i}$. Compute $\hat{r}$ and $Cov(\hat{r})$ as

$$\hat{r} = \sum_{j \in I_R} \sum_{i=1}^{N(Q_j)-2} \frac{\vec{r}_{j,i}}{m_R} \tag{28}$$

$$\text{Cov}(\hat{r}) = \sum_{j \in I_R} \sum_{i=1}^{N(Q_j)-2} \frac{(\vec{r}_{j,i} - \hat{r})(\vec{r}_{j,i} - \hat{r})^t}{m_R \cdot (m_R - 1)} \tag{29}$$

where $m_R = \sum_{j \in I_R} (N(Q_j) - 2)$.

Step 3: Construct $R_C[\vec{q}|m+2]$ and $\vec{p}_C[\vec{q}|m+2]$ as

$$R_C[\vec{q}|m+2] = \begin{bmatrix} {}_0R_{n,1} - {}_0R_{n,2} \\ \vdots \\ {}_0R_{n,m+1} - {}_0R_{n,m+2} \end{bmatrix}$$

$$\vec{p}_C[\vec{q}|m+2] = \begin{bmatrix} \vec{p}_R(Q_2) - \vec{p}_R(Q_1) \\ \vdots \\ \vec{p}_R(Q_{m+2}) - \vec{p}_R(Q_{m+1}) \end{bmatrix}$$

where

$$\vec{p}_R(Q_j) = \sum_{i=1}^{N(Q_j)} \left({}_0R_{n,j}\, \hat{\mathcal{X}}\, {}_s\vec{p}_\phi(\vec{q}_{j,i}) + {}_0\vec{p}_n(\vec{q}_{j,i}) \right) / N(Q_j).$$

Step 4: Compute $\hat{x}$ and $\text{Cov}(\hat{x})$ using

$$\hat{x} = (R_C[\vec{q}|m+2]^t R_C[\vec{q}|m+2])^{-1} \cdot R_C[\vec{q}|m+2]^t \vec{p}_C[\vec{q}|m+2] \tag{30}$$

$$\text{Cov}(\hat{x}) = (R_C[\vec{q}|m+2]^t R_C[\vec{q}|m+2])^{-1} \cdot \hat{\sigma}^2 \tag{31}$$

$$\hat{\sigma}^2 = \frac{\|\vec{p}_C[\vec{q}|m+2] - R_C[\vec{q}|m+2]\,\hat{x}\|^2}{3 \cdot (m+1)}. \tag{32}$$

VI. Simulation and Experiment Results

Simulations and experiments have been carried out. They are presented in Subsections VI-A and VI-B, respectively.

A. Simulations

The class A, B, and C calibration procedures have been implemented. Simulation data, both error-free and contaminated, are used to evaluate their performances. While the error-free data produce calibration results of negligible inaccuracies caused by rounding errors of the host computer, the contaminated data yield consistent calibration results. In this subsection, the data-generating process is described first. Then simulation results are presented.

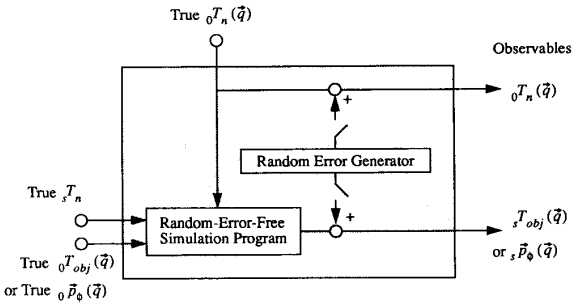

Fig. 9. Diagram of the simulation program.

TABLE II
Standard Deviations of Random Errors for Elements of ${}_0\vec{t}_n(\vec{q})$ and ${}_s\vec{t}_\phi(\vec{q})$

Element	Standard Deviation
${}_0x_n(\vec{q})$	1.0% of $\lvert{}_0x_n(\vec{q})\rvert$
${}_0y_n(\vec{q})$	1.0% of $\lvert{}_0y_n(\vec{q})\rvert$
${}_0z_n(\vec{q})$	1.0% of $\lvert{}_0z_n(\vec{q})\rvert$
${}_0u_n(\vec{q})$	0.1°
${}_0v_n(\vec{q})$	0.1°
${}_0\theta_n(\vec{q})$	0.1°
${}_sx_\phi(\vec{q})$	10.0% of $\lvert{}_sx_\phi(\vec{q})\rvert$
${}_sy_\phi(\vec{q})$	10.0% of $\lvert{}_sy_\phi(\vec{q})\rvert$
${}_sz_\phi(\vec{q})$	10.0% of $\lvert{}_sz_\phi(\vec{q})\rvert$
${}_su_\phi(\vec{q})$	1.0°
${}_sv_\phi(\vec{q})$	1.0°
${}_s\theta_\phi(\vec{q})$	1.0°

1) The Data-Generating Process: The simulation program, as sketched in the block diagram of Fig. 9, generates observables of ${}_0T_n(\vec{q})$ and ${}_sT_\phi(\vec{q})$. It begins with reading in $\mathcal{X}$, ${}_0T_\phi$ and the true ${}_0T_n(\vec{q})$. Then the error-free ${}_sT_\phi(\vec{q})$ is calculated. Finally, random errors are added to the true ${}_0T_n(\vec{q})$ and error-free ${}_sT_\phi(\vec{q})$ when collecting contaminated samples. Otherwise, the random error generator is turned off.

To prevent unexpected factors from biasing performances of the calibration procedures, samples are collected from simulated systems of comparable parameters. The $\{n\}$-frame is restricted within a spherical work space having a radius of 5 length units, and the reference objects are 10 length units away from the $\{0\}$-frame, i.e., $\|{}_0\vec{p}_\phi\|$ = 10 length units. In addition, let ${}_0\vec{t}_n(\vec{q}) = ({}_0u_n(\vec{q}), {}_0v_n(\vec{q}), {}_0\theta_n(\vec{q}), {}_0x_n(\vec{q}), {}_0y_n(\vec{q}), {}_0z_n(\vec{q}))^t$ and ${}_s\vec{t}_\phi(\vec{q}) = ({}_su_\phi(\vec{q}), {}_sv_\phi(\vec{q}), {}_s\theta_\phi(\vec{q}), {}_sx_\phi(\vec{q}), {}_sy_\phi(\vec{q}), {}_sz_\phi(\vec{q}))^t$ be the vector representations of ${}_0T_n(\vec{q})$ and ${}_sT_\phi(\vec{q})$, respectively. The measurement errors associated with components of observables ${}_0\vec{t}_n(\vec{q})$ and ${}_s\vec{t}_\phi(\vec{q})$ are normally distributed with trivial means. Their standard deviations are given in Table II. The error magnitudes of ${}_0\vec{t}_n(\vec{q})$ are assigned to be

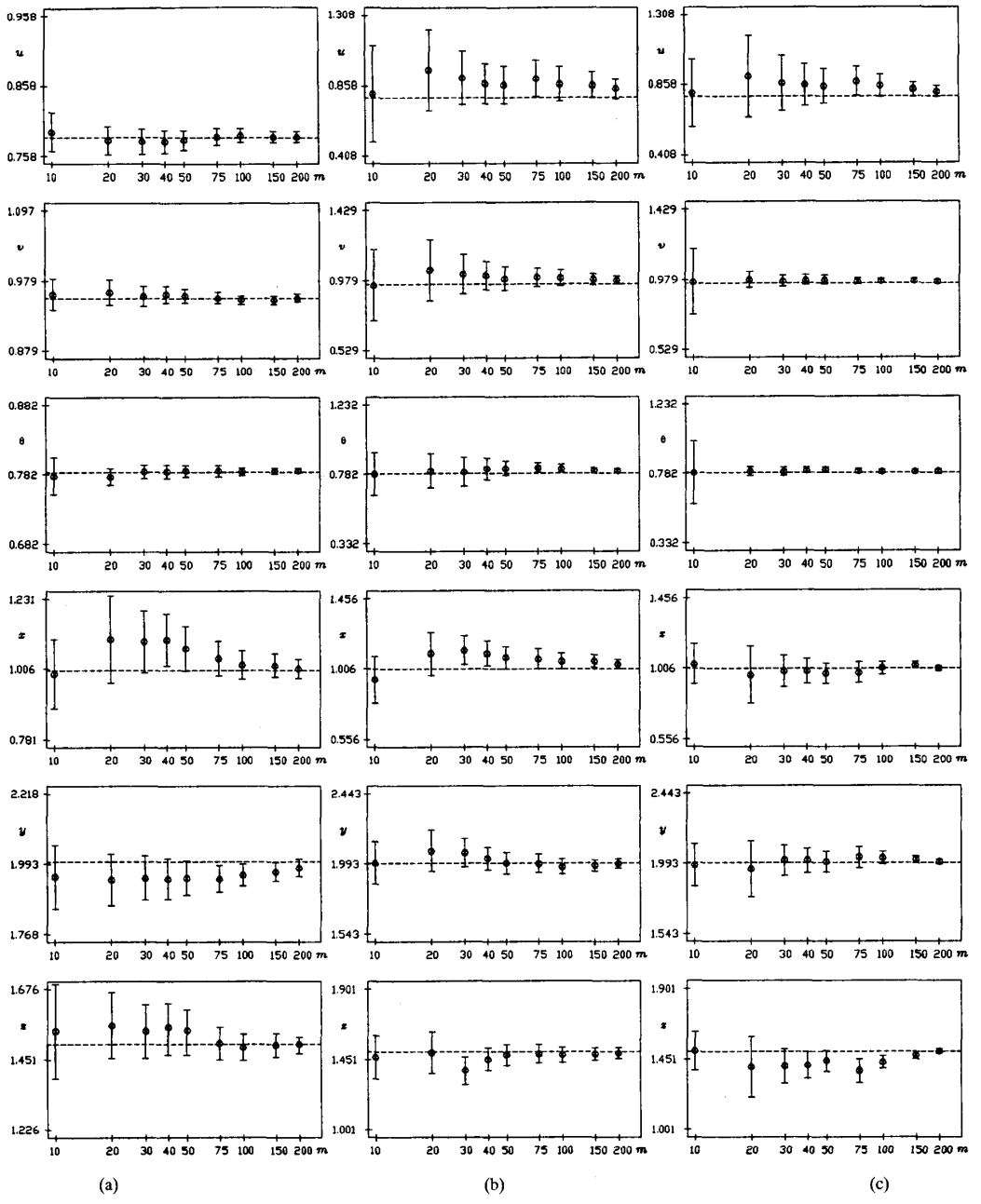

Fig. 10. Simulation results. (a) Class A procedure. (b) Class B procedure. (c) Class C procedure.

smaller than their counter parts of ${}_s\vec{t}_\phi(\vec{q})$ to reflect that the resolutions of ${}_0\vec{t}_n(\vec{q})$ obtained by forward kinematics are usually higher than those of ${}_s\vec{t}_\phi(\vec{q})$ obtained by the vision sensor.

2) Simulation Results: The class A procedure requires the precalibration of ${}_0T_\phi$. Therefore, in addition to samples of ${}_0T_n(\vec{q})$ and ${}_sT_\phi(\vec{q})$, ${}_0T_\phi$ is also input to the class A procedure. Calibration results of various sample sizes are presented in Fig. 10(a), where 95% confidence bars of the extrinsic parameters are plotted. It is observed that calibration results converge quickly to their corresponding true values. The class B procedure takes paired observations of ${}_0T_n(\vec{q})$ and ${}_sT_\phi(\vec{q})$. Calibration results are presented in Fig. 10(b). It shows that the point estimates converge to the true values consistently. In addition, standard deviations of estimates shrink while the sample size increases. The class C procedure takes samples of ${}_0T_n(\vec{q})$ and ${}_s\vec{p}_\phi(\vec{q})$. The extrinsic parameters, as plotted in Fig. 10(c), consistently converge to their corresponding true values. Standard deviations of estimates shrink faster than those of the class B procedure as the sample size increases.

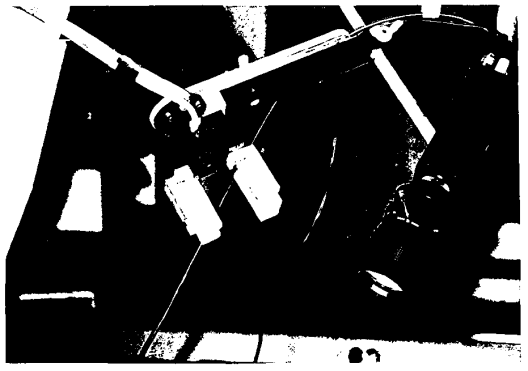

Fig. 11. The hand/eye setup.

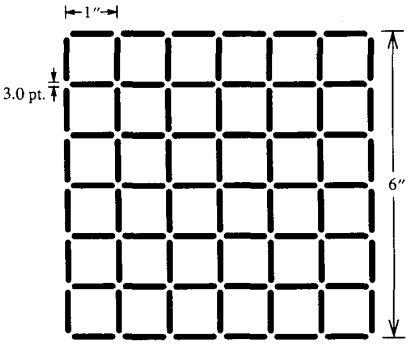

Fig. 12. The 2-D calibration template for testing the class B calibration procedure.

B. Experiments

The class A calibration procedure yields biased results unless the error-free ${}_0T_\phi$ is specified. Unfortunately, the error-free ${}_0T_\phi$ can hardly be identified. Therefore, the class B and C, but not A, calibration procedures have been tested. In the sequel, the hand/eye setup is described first. Then tests of the class B and C procedures are presented separately.

1) The Hand/Eye Setup: A PULNiX TM 540 CCD camera is mounted on the last link of a PUMA 560 robot as shown in Fig. 11. The camera has a 510 × 490 sensor array and a National LMZ13Z5M/12Z6H zoom lens. It is supported by an Image Technology's Series 151 image processor and an IBM PS/2 model 70-E61 personal computer. The uncertainty scale factor s_x and the image center $(c_x, c_y)^t$ have been determined using methods outlined in Appendixes V and VI, respectively.

2) Test of the Class B Calibration Procedure: Identifying the reference object's pose from its image is a prerequisite of the class B calibration procedure. Two methods exist: the versatile camera calibration technique [33] and the monocular pose acquisition method [37]. Both, while acquiring the effective focal length and the reference object's pose, need no iterative searches. The monocular pose acquisition method is employed, of which the reference object can be either a 2-D rectangular or a 3-D cuboid. A 2-D grid template as shown in Fig. 12 is used. The template is printed on a 3M transparent sheet using an NEC laser printer of 300× 300 dpi resolution. The intersection points of parallel and perpendicular line segments, as identified on the image plane, are used to identify ${}_sT_\phi(\vec{q})$. The pattern of line segments eases the image processing burden, whereas the multiplicity of grids improves the accuracy of the acquired pose.

Table III lists results obtained by the class B calibration procedure, where m_s is the sample size. For comparison, methods explored by Tsai and Lenz [34] and Shiu and Ahmad [29] have also been implemented. Their results are listed in Tables IV and V, respectively. Individually, every method appears to have produced consistent results. Collectively, their results are consistent, too. The corresponding 95% confidence intervals, calculated at $m_s = 10$, overlap each other. However, the class B and the Tsai–Lenz methods have obtained smaller standard deviations than those by the Shiu–Ahmad method.

TABLE III
EXPERIMENTAL RESULTS OF THE CLASS B EXTRINSIC CALIBRATION PROCEDURE (u, v, θ ARE IN RADIANS AND x, y, z ARE IN INCHES.)

m_s	$u\|\sigma_u$	$v\|\sigma_v$	$\theta\|\sigma_\theta$	$x\|\sigma_x$	$y\|\sigma_y$	$z\|\sigma_z$
4	1.506|0.010	1.619|0.012	0.649|0.014	-5.25|0.26	-7.74|0.31	6.32|0.24
6	1.532|0.017	1.625|0.007	0.669|0.021	-5.71|0.26	-7.95|0.40	6.54|0.25
8	1.500|0.022	1.611|0.016	0.650|0.023	-5.38|0.16	-7.82|0.26	6.37|0.15
10	1.501|0.018	1.618|0.013	0.636|0.020	-5.17|0.12	-7.95|0.20	6.36|0.11

TABLE IV
EXPERIMENTAL RESULTS OF THE TSAI–LENZ EXTRINSIC CALIBRATION METHOD (u, v, θ ARE IN RADIANS AND x, y, z ARE IN INCHES.)

m_s	$u\|\sigma_u$	$v\|\sigma_v$	$\theta\|\sigma_\theta$	$x\|\sigma_x$	$y\|\sigma_y$	$z\|\sigma_z$
4	1.488|0.000	1.629|0.006	0.624|0.000	-4.84|0.14	-7.61|0.17	6.23|0.13
6	1.511|0.017	1.636|0.010	0.661|0.023	-5.57|0.20	-7.79|0.30	6.51|0.19
8	1.499|0.013	1.632|0.007	0.646|0.018	-5.32|0.14	-7.81|0.23	6.36|0.14
10	1.493|0.011	1.630|0.006	0.639|0.014	-5.23|0.11	-7.87|0.19	6.41|0.10

TABLE V
EXPERIMENTAL RESULTS OF THE SHIU– AHMAD EXTRINSIC CALIBRATION METHOD (u, v, θ ARE IN RADIANS AND x, y, z ARE IN INCHES.)

m_s	$u\|\sigma_u$	$v\|\sigma_v$	$\theta\|\sigma_\theta$	$x\|\sigma_x$	$y\|\sigma_y$	$z\|\sigma_z$
4	1.615|0.129	1.773|0.078	0.622|0.001	-4.77|0.69	-8.60|0.82	6.17|0.63
6	1.539|0.076	1.631|0.100	0.661|0.024	-5.61|0.25	-8.01|0.39	6.49|0.25
8	1.558|0.052	1.646|0.074	0.646|0.018	-5.37|0.25	-8.24|0.40	6.36|0.24
10	1.574|0.048	1.668|0.064	0.641|0.014	-5.27|0.25	-8.51|0.43	6.41|.023

On average, the Tsai–Lenz method has produced calibration results of the smallest standard deviations.

3) Test of the Class C Calibration Procedure: The reference point of the class C calibration procedure can be either the center of a circular disk or the intersection point of two lines. To locate the disk center on the image plane, as discussed in Appendix VII, may not be easy. The template of four disconnected line segments, as shown in Fig. 13, is adopted. The pattern of disconnected line segments eases the image processing burden, whereas line segments of excessive length elevate the accuracy of the identified intersection point on the image plane.

${}_s\vec{p}_\phi(\vec{q})$ cannot be resolved from a single observation. However, it can be recovered from a minimum of four samples

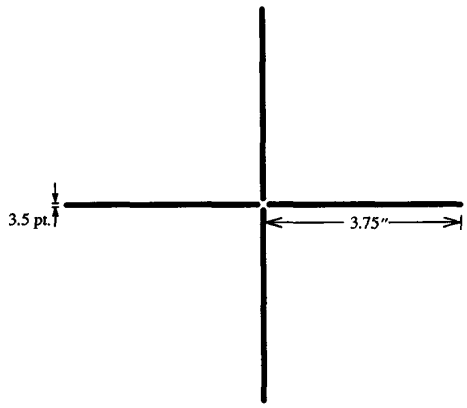

Fig. 13. The 2-D calibration template for testing the class C calibration procedure.

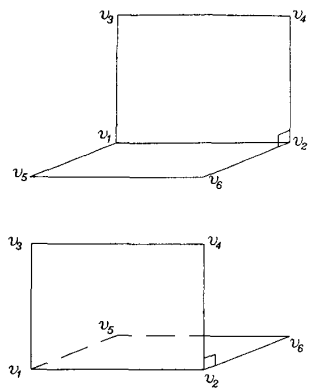

Fig. 14. Structured manipulator configurations for testing the class C calibration procedure.

taken at structured positions. Let V_i, $i \in I_4$ be the vertices of a 2-D rectangular inside the robot work space. Locate the origin of the $\{n|\vec{q}_i\}$-frame at V_i while keeping ${}_0R_n(\vec{q}_i)$ fixed for $i \in I_4$. In a sequence, record the reference point's image. By relative motions, the reference point appears to be at the vertices of a rectangle similar to the one defined by V_i, $i \in I_4$. Therefore, the pose acquisition method is eligible for identifying the translation vectors ${}_s\vec{p}_\phi(\vec{q}_i)$, $i \in I_4$. To enhance accuracy, samples have been collected on V_i, $i \in I_6$, where V_i as plotted in Fig. 14 are on two perpendicular planes. Calibration results, which appear consistent with and comparable to previous ones, are summarized in Table VI.

TABLE VI
EXPERIMENTAL RESULTS OF THE CLASS C EXTRINSIC CALIBRATION PROCEDURE (u, v, θ ARE IN RADIANS AND x, y, z ARE IN INCHES.)

m_s	$u\|\sigma_u$	$v\|\sigma_v$	$\theta\|\sigma_\theta$	$x\|\sigma_x$	$y\|\sigma_y$	$z\|\sigma_z$
4	1.439|0.018	1.657|0.026	0.648|0.030	-4.73|0.27	-8.28|0.28	6.59|0.16
6	1.457|0.017	1.654|0.024	0.620|0.027	-4.63|0.18	-8.33|0.18	6.33|0.19
8	1.476|0.019	1.653|0.027	0.621|0.020	-4.73|0.15	-8.37|0.14	6.25|0.15
10	1.472|0.015	1.645|0.022	0.617|0.017	-4.74|0.13	-8.47|0.13	6.31|0.13

VII. SUMMARY AND DISCUSSIONS

Three classes of extrinsic calibration procedures have been presented. All use closed-form solutions. By simulations and field experiments, they have proven to yield estimates converging to true extrinsic parameter values. The class A calibration procedure requires a well-structured reference object at a precalibrated location. The class B calibration procedure also requires a well-structured reference object but not precalibration. While the class B calibration procedure takes advantage of robot mobility, the class C calibration procedure takes full advantage of robot mobility and dexterity. It requires no reference object but the simplest one—a single visible point.

The class B calibration method and two existing methods, Tsai and Lenz's and Shiu and Ahmad's methods, have been experimentally compared. The class B and the Tsai–Lenz methods have obtained better results than the Shiu–Ahmad method. On average, the Tsai–Lenz method has yielded the best results.

Ideally, the mounting position of a range-finding sensor, i.e., [14], [15], would be calibrated under an error-free environment. The class A calibration procedure takes one observation of the reference frame, or equivalently three vertex observations, to determine the mounting position. The class B calibration procedure needs three observations of the reference frame, a total of nine vertex observations. The class C calibration procedure requires a minimum of five observations of the reference point, three for $\mathcal{X}$ followed by two for $\vec{x}$. In comparison, the class A calibration procedure has the highest data efficiency. However, the class A calibration procedure risks producing biased results unless the precalibration is free of errors. The data efficiency of the class C calibration procedure is better than that of the class B calibration procedure.

The class A, B, and C calibration procedures are eligible for the extrinsic calibration among sensors of a stereo vision system should it be mounted on a dexterous spatial positioning mechanism. First, identify the homogeneous transform between every individual sensor and the mounted link. Then calculate the homogeneous transforms among sensor frames using the transformation arithmetics.

APPENDIX I
SOLUTIONS OF ${}_{n_i}R_{n_\varrho}\mathcal{X} = \mathcal{X}\,{}_{s_i}R_{s_\varrho}$, $\varrho \in \{j,k\}$

Collect samples of ${}_0T_n(\vec{q})$ and ${}_sT_\phi(\vec{q})$ at $\vec{q}_i$, $\vec{q}_j$ and $\vec{q}_k$. Calculate ${}_{n_i}T_{n_\varrho}$ and ${}_{s_i}T_{s_\varrho}$ for $\varrho \in \{j,k\}$. Then $\mathcal{X} \in \{R|R\ {}_{s_i}\vec{k}_{s_j} = {}_{n_i}\vec{k}_{n_j}\} \cap \{R|R\ {}_{s_i}\vec{k}_{s_k} = {}_{n_i}\vec{k}_{n_k}\}$ by Theorem 2. There exist two experimental options: either ${}_{n_i}\vec{k}_{n_j} = \pm\,{}_{n_i}\vec{k}_{n_k}$, i.e., ${}_{n_i}\vec{k}_{n_j}$ is parallel or antiparallel to ${}_{n_i}\vec{k}_{n_k}$, or ${}_{n_i}\vec{k}_{n_j} \neq \pm\,{}_{n_i}\vec{k}_{n_k}$, i.e., ${}_{n_i}\vec{k}_{n_j}$ is not parallel nor antiparallel to ${}_{n_i}\vec{k}_{n_k}$. The option of ${}_{n_i}\vec{k}_{n_j} \neq \pm\,{}_{n_i}\vec{k}_{n_k}$ warrants that the intersection set $\{R|R\ {}_{s_i}\vec{k}_{s_j} = {}_{n_i}\vec{k}_{n_j}, R\ {}_{s_i}\vec{k}_{s_k} = {}_{n_i}\vec{k}_{n_k}\}$ contains the single element $\mathcal{X}$. It constitutes the normal experimental condition. On the other hand, the option of ${}_{n_i}\vec{k}_{n_j} = \pm\,{}_{n_i}\vec{k}_{n_k}$ constitutes the undesirable experimental condition. It makes $\{R|R\ {}_{s_i}\vec{k}_{s_j} = {}_{n_i}\vec{k}_{n_k}\} = \{R|R\ {}_{s_i}\vec{k}_{s_k} = {}_{n_i}\vec{k}_{n_k}\}$. Hence, $\mathcal{X}$ remains at large. They are distinguished in the following discussions. First $\mathcal{X}$ is resolved for the normal experimental

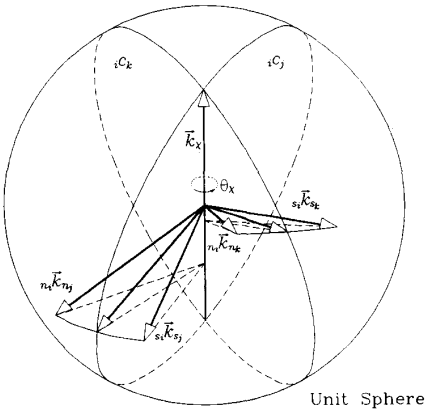

(a)

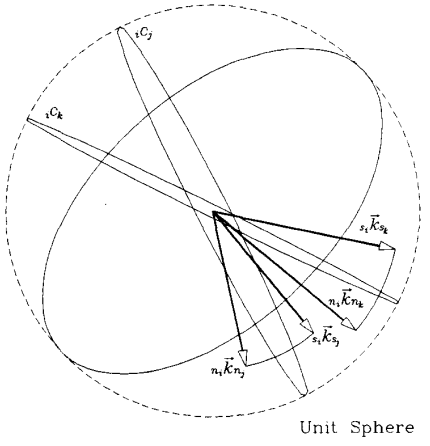

(b)

Fig. 15. ${}_iC_j$ and ${}_iC_k$ uniquely determine $\vec{k}_{\mathcal{X}}$. (a) Side view. (b) Top view.

condition. Then the reason for ${}_{n_i}\vec{k}_{n_j} = \pm {}_{n_i}\vec{k}_{n_k}$ constituting the undesirable experimental condition is briefly addressed.

A. Normal Experimental Condition: ${}_{n_i}\vec{k}_{n_j} \neq \pm {}_{n_i}\vec{k}_{n_k}$

When ${}_{n_i}\vec{k}_{n_j} \neq \pm {}_{n_i}\vec{k}_{n_k}$, the following four cases exist:

Case 1: ${}_{n_i}\vec{k}_{n_j} \neq {}_{s_i}\vec{k}_{s_j}$ and ${}_{n_i}\vec{k}_{n_k} \neq {}_{s_i}\vec{k}_{s_k}$,
Case 2: ${}_{n_i}\vec{k}_{n_j} = {}_{s_i}\vec{k}_{s_j}$ and ${}_{n_i}\vec{k}_{n_k} \neq {}_{s_i}\vec{k}_{s_k}$,
Case 3: ${}_{n_i}\vec{k}_{n_j} \neq {}_{s_i}\vec{k}_{s_j}$ and ${}_{n_i}\vec{k}_{n_k} = {}_{s_i}\vec{k}_{s_k}$,
Case 4: ${}_{n_i}\vec{k}_{n_j} = {}_{s_i}\vec{k}_{s_j}$ and ${}_{n_i}\vec{k}_{n_k} = {}_{s_i}\vec{k}_{s_k}$.

Solutions of $\mathcal{X}$ are derived below in numbered order.

Case 1. ${}_{n_i}\vec{k}_{n_j} \neq {}_{s_i}\vec{k}_{s_j}$ *and* ${}_{n_i}\vec{k}_{n_k} \neq {}_{s_i}\vec{k}_{s_k}$*:* Two subcases, the regular subcase of ${}_iC_j \neq {}_iC_k$ and the special subcase of ${}_iC_j = {}_iC_k$, are distinguished. They are shown in Figs. 15(a)–(b) and 16, respectively. The regular subcase happens most of the time, whereas the special subcase occurs only by chance.

Case 1.1. ${}_iC_j \neq {}_iC_k$*:* In this regular subcase, $\vec{k}_{\mathcal{X}}$, as shown in Fig. 15(a) (side view) and (b) (top view), is obtained

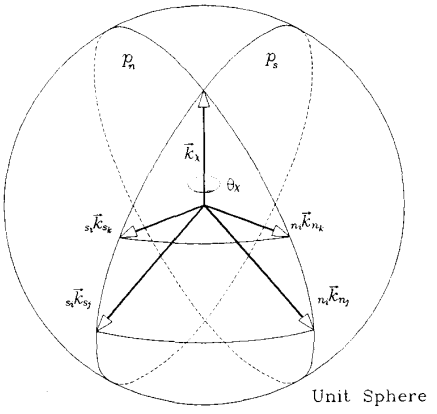

Fig. 16. P_s and P_n planes uniquely determine $\vec{k}_{\mathcal{X}}$.

by solving the following simultaneous equations:

$$({}_{n_i}\vec{k}_{n_\varrho} - {}_{s_i}\vec{k}_{s_\varrho})^t \vec{k}_{\mathcal{X}} = 0$$
$$\|\vec{k}_{\mathcal{X}}\| = 1, \ \varrho \in \{j, k\}. \tag{A1}$$

Since $({}_{n_i}\vec{k}_{n_j} - {}_{s_i}\vec{k}_{s_j}) \neq \pm({}_{n_i}\vec{k}_{n_k} - {}_{s_i}\vec{k}_{s_k})$ whenever ${}_iC_j \neq {}_iC_k$, $\vec{k}_{\mathcal{X}}$ is obtained as follows:

$$\vec{k}_{\mathcal{X}} = \pm \frac{({}_{n_i}\vec{k}_{n_j} - {}_{s_i}\vec{k}_{s_j}) \times ({}_{n_i}\vec{k}_{n_k} - {}_{s_i}\vec{k}_{s_k})}{\|({}_{n_i}\vec{k}_{n_j} - {}_{s_i}\vec{k}_{s_j}) \times ({}_{n_i}\vec{k}_{n_k} - {}_{s_i}\vec{k}_{s_k})\|}. \tag{A2}$$

The solutions of + and − signs represent identical solution. Only the one of the + sign is retained.

Once $\vec{k}_{\mathcal{X}}$ is resolved, $\theta_{\mathcal{X}}$, the generalized rotation angle of $\mathcal{X}$, is identified as follows:

$$\theta_{\mathcal{X}} = 2\,\mathrm{sgn}(\zeta_\varrho^i)\,\tan^{-1}\left(\frac{\|{}_{n_i}\vec{k}_{n_\varrho} - {}_{s_i}\vec{k}_{s_\varrho}\|}{\|\vec{k}_{\mathcal{X}} \times ({}_{n_i}\vec{k}_{n_\varrho} + {}_{s_i}\vec{k}_{s_\varrho})\|}\right),$$
$$\varrho = \text{ either } j \text{ or } k, \text{ and}$$
$$\max_{\varrho \in \{j,k\}} : \{|\cos^{-1}({}_{n_i}\vec{k}^t_{n_\varrho}\,{}_{s_i}\vec{k}_{s_\varrho})|\} \leq |\theta_{\mathcal{X}}| \leq \pi \tag{A3}$$

where sgn(·) is the sign function, i.e., $\mathrm{sgn}(\zeta) = 1$ if $\zeta \geq 0$ and $\mathrm{sgn}(\zeta) = -1$ if $\zeta < 0$, and $\zeta_\varrho^i = ({}_{n_i}\vec{k}_{n_\varrho} - {}_{s_i}\vec{k}_{s_\varrho})^t\left(\vec{k}_{\mathcal{X}} \times ({}_{n_i}\vec{k}_{n_\varrho} + {}_{s_i}\vec{k}_{s_\varrho})\right)$.

It is noted that choosing $\varrho =$ either j or k in (A3) yields the same value of $\theta_{\mathcal{X}}$ should no measurement errors be present. Unfortunately, random errors exist and introduce calibration inaccuracies. Equation (A3) does not yield identical values for both $\varrho = j$ and k. As a common practice, the average of those two values is used to estimate $\theta_{\mathcal{X}}$.

Case 1.2 ${}_iC_j = {}_iC_k$*:* In this special subcase $({}_{n_i}\vec{k}_{n_j} - {}_{s_i}\vec{k}_{s_j})$ is parallel with $({}_{n_i}\vec{k}_{n_k} - {}_{s_i}\vec{k}_{s_k})$. The denominator on the right-hand side of (A2) is trivial and (A2) becomes inapplicable. Fig. 16 illustrates the subcase. ${}_{n_i}\vec{k}_{n_j}$ and ${}_{n_i}\vec{k}_{n_k}$ are on one plane $\boldsymbol{P_n}$, ${}_{s_i}\vec{k}_{s_j}$ and ${}_{s_i}\vec{k}_{s_k}$ are on another plane $\boldsymbol{P_s}$ and $\vec{k}_{\mathcal{X}} \in \boldsymbol{P}_n \cap \boldsymbol{P}_s$. Therefore, $\vec{k}_{\mathcal{X}}$ and $\theta_{\mathcal{X}}$ are resolved as follows:

$$\vec{k}_{\mathcal{X}} = -({}_{n_i}\vec{k}_{n_j} \times {}_{n_i}\vec{k}_{n_k}) \times ({}_{s_i}\vec{k}_{s_j} \times {}_{s_i}\vec{k}_{s_k}) \tag{A4}$$

$$\theta_{\mathcal{X}} = \cos^{-1}\Big(({}_{n_i}\vec{k}_{n_j} \times {}_{n_i}\vec{k}_{n_k})^t({}_{s_i}\vec{k}_{s_j} \times {}_{s_i}\vec{k}_{s_k})\Big), \quad 0 \le \theta_{\mathcal{X}} \le \pi. \tag{A5}$$

Case 2. ${}_{n_i}\vec{k}_{n_j} = {}_{s_i}\vec{k}_{s_j}$ *and* ${}_{n_i}\vec{k}_{n_k} \neq {}_{s_i}\vec{k}_{s_k}$*:* In this case, Corollary 2.1 discloses that $\vec{k}_{\mathcal{X}} = {}_{n_i}\vec{k}_{n_j} = {}_{s_i}\vec{k}_{s_j}$, and $\theta_{\mathcal{X}}$ is obtained using (A3) with $\varrho = k$.

Case 3. ${}_{n_i}\vec{k}_{n_j} \neq {}_{s_i}\vec{k}_{s_j}$ *and* ${}_{n_i}\vec{k}_{n_k} = {}_{s_i}\vec{k}_{s_k}$*:* Corollary 2.1 discloses that $\vec{k}_{\mathcal{X}} = {}_{n_i}\vec{k}_{n_j} = {}_{s_i}\vec{k}_{s_j}$, and $\theta_{\mathcal{X}}$ is obtained using (A3) with $\varrho = j$.

Case 4. ${}_{n_i}\vec{k}_{n_j} = {}_{s_i}\vec{k}_{s_j}$ *and* ${}_{n_i}\vec{k}_{n_k} = {}_{s_i}\vec{k}_{s_k}$*:* Corollary 2.1 discloses that $\mathcal{X} = I_{3\times 3}$.

B. Undesirable Experimental Condition: ${}_{n_i}\vec{k}_{n_j} = \pm {}_{n_i}\vec{k}_{n_k}$

Theorem 1 discloses that ${}_{n_i}\vec{k}_{n_j}$ and ${}_{s_i}\vec{k}_{s_j}$ represents the same generalized axis of rotation in the $\{n|\vec{q}_i\}$-frame and $\{s|\vec{q}_i\}$-frame. Therefore, ${}_{n_i}\vec{k}_{n_j} = \pm {}_{n_i}\vec{k}_{n_k}$ if and only if ${}_{s_i}\vec{k}_{s_j} = \pm {}_{s_i}\vec{k}_{s_k}$. ${}_{n_i}R_{n_k}$ and ${}_{s_i}R_{s_k}$ offer no extra information for resolving $\mathcal{X}$ other than ${}_{n_i}R_{n_j}$ and ${}_{s_i}R_{s_j}$ do should ${}_{n_i}\vec{k}_{n_j} = \pm {}_{n_i}\vec{k}_{n_k}$ occur. The undesirable experimental condition can and should be avoided.

Appendix II
Sensitivity Analysis for $\vec{k}_{\mathcal{X}}$ and $\theta_{\mathcal{X}}$

An observer $\{o\}$-frame, in which $\mathcal{X}$ appears to be $\mathrm{Rot}(\vec{z}_o, \theta_{\mathcal{X}})$, is introduced to keep the sensitivity analysis evident. Such an observer frame, characterized by ${}_nR_o\,\vec{k}_{\mathcal{X}} = (0, 0, 1)^t$, always exists. As shown in Fig. 7, ${}_{n_\alpha}\vec{k}_{n_\beta}$ and ${}_{s_\alpha}\vec{k}_{s_\beta}$ are on the same latitude of a spinning sphere whose rotation axis is $\vec{z}_o$. Let $({}_{n_\alpha}u_{n_\beta}, {}_{n_\alpha}v_{n_\beta})$ define ${}_{n_\alpha}\vec{k}_{n_\beta}$ in the $\{o\}$-frame. Then $({}_{n_\alpha}u_{n_\beta} + \theta_{\mathcal{X}}, {}_{n_\alpha}v_{n_\beta})$ represents ${}_{s_\alpha}\vec{k}_{s_\beta}$.

The value of $\vec{k}_{\mathcal{X}}$ in (5) is sensitive to random errors when the true value of the denominator on the right hand side is approaching 0. Since

$$\begin{aligned}\|({}_{n_i}\vec{k}_{n_j} - {}_{s_i}\vec{k}_{s_j}) \times ({}_{n_i}\vec{k}_{n_k} - {}_{s_i}\vec{k}_{s_k})\| &= 4\sin(|{}_{n_i}u_{n_j} - {}_{n_i}u_{n_k}|)\sin(|{}_{n_i}v_{n_j}|) \\ &\quad \cdot \sin(|{}_{n_i}v_{n_k}|)\sin^2\left(\left|\frac{\theta_{\mathcal{X}}}{2}\right|\right).\end{aligned} \tag{B1}$$

$\vec{k}_{\mathcal{X}}$ is sensitive to random errors should any of the following four unstable conditions arise:

1) $|{}_{n_i}u_{n_j} - {}_{n_i}u_{n_k}| \to 0$ or π;
2) $|{}_{n_i}v_{n_j}| \to 0$ or π;
3) $|{}_{n_i}v_{n_k}| \to 0$ or π;
4) $|\theta_{\mathcal{X}}| \to 0$.

$\theta_{\mathcal{X}}$, in both magnitude and sign, is sensitive if $\vec{k}_{\mathcal{X}}$ is unstable or $\|\vec{k}_{\mathcal{X}} \times ({}_{n_i}\vec{k}_{n_\varrho} + {}_{s_i}\vec{k}_{s_\varrho})\|$, $\varrho \in \{j, k\}$, are small. Therefore, the following two additional conditions also make $\theta_{\mathcal{X}}$ sensitive to random errors:

5) $\theta_{\mathcal{X}} \to \pi$ and ${}_{n_i}v_{n_\varrho} \to \frac{\pi}{2}$, $\varrho \in \{j, k\}$;
6) ${}_{n_i}v_{n_\varrho} \to 0$ or π, $\varrho \in \{j, k\}$.

While $\vec{k}_{\mathcal{X}}$ and $\theta_{\mathcal{X}}$ are sensitive to random errors under the above six unstable conditions, they are most insensitive to random errors when $|{}_{n_i}u_{n_k} - {}_{n_i}u_{n_j}| = \pi/2$, $|{}_{n_i}v_{n_\varrho}| = \pi/2$, $\varrho \in \{j, k\}$, and $|\theta_{\mathcal{X}}| = \pi/2$, *i.e.*, ${}_{n_i}\vec{k}_{n_j}^t\vec{k}_{\mathcal{X}} = 0$, ${}_{n_i}\vec{k}_{n_k}^t\vec{k}_{\mathcal{X}} = 0$, ${}_{n_i}\vec{k}_{n_j}^t{}_{n_i}\vec{k}_{n_k} = 0$ and $|\theta_{\mathcal{X}}| = \pi/2$. The stable and unstable conditions of $\vec{k}_{\mathcal{X}}$ and $\theta_{\mathcal{X}}$ have been confirmed by numerical evaluations.

Appendix III
Distances Between Rotation Matrices

Let $\hat{\mathcal{X}}$ and $\hat{x}$ be the respective estimates of $\mathcal{X}$, a 3×3 rotation matrix, and $\vec{x}$, a 3×1 translation vector. Traditionally, the 2-norm of $\|\hat{x} - \vec{x}\|$ is used to assess the inaccuracy of $\hat{x}$. However, it is inapplicable to rotation matrices [34]. This appendix presents two eligible measurements. Let $E = \{\vec{e} \mid \|\vec{e}\| = 1\}$. Then $\|(R_\alpha - R_\beta)\vec{e}\|$, $\vec{e} \in E$ is the Euclidean distance between head ends of unit vectors $R_\alpha\vec{e}$ and $R_\beta\vec{e}$ that span an angle of $\cos^{-1}((R_\alpha\vec{e})^tR_\beta\vec{e})$. Define

$$\mathcal{N}(R_\alpha, R_\beta) = \max_{\vec{e}\in E}\{\|(R_\alpha - R_\beta)\vec{e}\|\} \tag{C1}$$

$$\mathcal{A}(R_\alpha, R_\beta) = \max_{\vec{e}\in E}\{|\cos^{-1}((R_\alpha\vec{e})^tR_\beta\vec{e})|\}. \tag{C2}$$

Both consistently gauge the distance between R_α and R_β. In addition, their evaluations require no lengthy calculation as disclosed by the following theorem, which is proved in Appendix IV.

Theorem 4: Let $R_\alpha = \mathrm{Rot}(\vec{k}_\alpha, \theta_\alpha)$, $R_\beta = \mathrm{Rot}(\vec{k}_\beta, \theta_\beta)$ and $R_\beta^{-1}R_\alpha = \mathrm{Rot}(\vec{k}_{\alpha\times\beta}, \theta_{\alpha\times\beta})$. Then $\mathcal{N}(R_\alpha, R_\beta) = 2\sin(|\theta_{\alpha\times\beta}|/2)$ and $\mathcal{A}(R_\alpha, R_\beta) = |\theta_{\alpha\times\beta}|$.

It is noted that $\mathcal{N}(R_\alpha, R_\beta)$, as well as $\mathcal{A}(R_\alpha, R_\beta)$, is trivial if and only if $R_\alpha = R_\beta$.

The Euclidean distance $\|\hat{x} - \vec{x}\|$ has been used to measure the distance by which $\hat{x}$ misses $\vec{x}$. That tradition is honored and $\mathcal{N}(\hat{\mathcal{X}}, \mathcal{X})$ is used to assess the inaccuracy of $\hat{\mathcal{X}}$ although it takes one multiplication, one division, and one sine function evaluation beyond the calculation of $\mathcal{A}(\hat{\mathcal{X}}, \mathcal{X})$.

Appendix IV
Theorems and Proofs

Theorem 1: Let ${}_{n_1}R_{n_2} = \mathrm{Rot}({}_{n_1}\vec{k}_{n_2}, {}_{n_1}\theta_{n_2})$ and ${}_{s_1}R_{s_2} = \mathrm{Rot}({}_{s_1}\vec{k}_{s_2}, {}_{s_1}\theta_{s_2})$. Then ${}_{n_1}\vec{k}_{n_2}$ and ${}_{s_1}\vec{k}_{s_2}$ represent the same vector in the $\{n|\vec{q}_1\}$-frame and the $\{s|\vec{q}_1\}$-frame. Furthermore, ${}_{n_1}\theta_{n_2} = {}_{s_1}\theta_{s_2}$.

Proof: ${}_{n_1}R_{n_2}$ rotates the orientation of the $\{n|\vec{q}_2\}$-frame into that of the $\{n|\vec{q}_1\}$-frame. ${}_{s_1}R_{s_2}$ turns the orientation of the $\{s|\vec{q}_2\}$-frame into that of the $\{s|\vec{q}_1\}$-frame. ${}_{n_1}R_{n_2}$ and ${}_{s_1}R_{s_2}$ represent rotation operations caused by the change of manipulator configuration. Since the $\{s\}$-frame and the $\{n\}$-frame are fixed to each other, ${}_{n_1}R_{n_2}$ and ${}_{s_1}R_{s_2}$ are representations of the same rotation operator in two different frames, i.e., the$\{n|\vec{q}_1\}$-frame and the $\{s|\vec{q}_1\}$-frame. Therefore, ${}_{n_1}\vec{k}_{n_2}$ and ${}_{s_1}\vec{k}_{s_2}$ represent the same generalized rotation axis in the $\{n|\vec{q}_1\}$-frame and the $\{s|\vec{q}_1\}$-frame. Furthermore, ${}_{n_1}\theta_{n_2} = {}_{s_1}\theta_{s_2}$ since the angle of rotation is a scalar that is invariant to the change of coordinate frames. □

Theorem 2: ${}_{n_1}R_{n_2}\,\mathcal{X} = \mathcal{X}\,{}_{s_1}R_{s_2}$ if and only if $\mathcal{X}\,{}_{s_1}\vec{k}_{s_2} = {}_{n_1}\vec{k}_{n_2}$.

Proof: ${}_{n_1}R_{n_2}\,\mathcal{X} = \mathcal{X}\,{}_{s_1}R_{s_2}$ and ${}_{s_1}R_{s_2}\,{}_{s_1}\vec{k}_{s_2} = {}_{s_1}\vec{k}_{s_2}$ yield ${}_{n_1}R_{n_2}\,\mathcal{X}\,{}_{s_1}\vec{k}_{s_2} = \mathcal{X}\,{}_{s_1}\vec{k}_{s_2}$. $\mathcal{X}\,{}_{s_1}\vec{k}_{s_2}$ is the eigenvector of ${}_{n_1}R_{n_2}$ having unity eigenvalue. Therefore, $\mathcal{X}\,{}_{s_1}\vec{k}_{s_2} = {}_{n_1}\vec{k}_{n_2}$.

Inversely, ${}^{\mathcal{X}}{}_{s_1}\vec{k}_{s_2} = {}_{n_1}\vec{k}_{n_2}$ results in $\mathrm{Rot}({}_{n_1}\vec{k}_{n_2}, {}_{n_1}\theta_{n_2}) = \mathrm{Rot}({}^{\mathcal{X}}{}_{s_1}\vec{k}_{s_2}, {}_{s_1}\theta_{s_2}) = {}^{\mathcal{X}}{}_{s_1}R_{s_2}\mathcal{X}^{-1}$. Hence, ${}_{n_1}R_{n_2}\mathcal{X} = \mathcal{X}\,{}_{s_1}R_{s_2}$. □

Corollary 2.1: Let ${}_{n_1}\vec{k}_{n_2} = {}_{s_1}\vec{k}_{s_2}$. Denote $\mathrm{Rot}(\vec{k}_{\mathcal{X}}, \theta_{\mathcal{X}})$ as the operator representation of $\mathcal{X}$. Then ${}_{n_1}R_{n_2}\mathcal{X} = \mathcal{X}\,{}_{s_1}R_{s_2}$ if and only if $\vec{k}_{\mathcal{X}} = {}_{n_1}\vec{k}_{n_2} = {}_{s_1}\vec{k}_{s_2}$ and $\mathcal{X} \in \{\mathrm{Rot}(\vec{k}_{\mathcal{X}}, \theta) | 0 < \theta < 2\pi\} \cup \{\mathrm{Rot}(\vec{k}, \theta_{\mathcal{X}}) | \, \|\vec{k}\| = 1, \theta_{\mathcal{X}} = 0\}$. Furthermore, $\mathcal{X} \in \{\mathrm{Rot}(\vec{k}_{\mathcal{X}}, \theta) | 0 < \theta < 2\pi\}$ when $\mathcal{X} \neq I_{3\times 3}$, and $\mathcal{X} \in \{\mathrm{Rot}(\vec{k}, \theta_{\mathcal{X}}) | \, \|\vec{k}\| = 1, \theta_{\mathcal{X}} = 0\}$ when $\mathcal{X} = I_{3\times 3}$.

Proof: Since the generalized rotation axis of $\mathcal{X}$ is the only unit vector having the same representation in both the $\{n|\vec{q}_1\}$-frame and the $\{s|\vec{q}_1\}$-frame, ${}_{n_1}\vec{k}_{n_2} = {}_{s_1}\vec{k}_{s_2}$ if and only if ${}_{n_1}\vec{k}_{n_2} = {}_{s_1}\vec{k}_{s_2} = \vec{k}_{\mathcal{X}}$. In addition, Theorem 2 reveals that ${}_{n_1}R_{n_2}\mathcal{X} = \mathcal{X}\,{}_{s_1}R_{s_2}$ if and only if $\mathcal{X} \in \{\mathrm{Rot}(\vec{k}_{\mathcal{X}}, \theta) | 0 \leq \theta < 2\pi\}$, of which $\mathcal{X} = I_{3\times 3} \in \{\mathrm{Rot}(\vec{k}, \theta_{\mathcal{X}}) | \, \|\vec{k}\| = 1, \theta_{\mathcal{X}} = 0\}$ is a special case. □

Theorem 3: $R_B[\vec{q}|3]$ is of full rank if and only if ${}_{n_1}\vec{k}_{n_2} \neq \pm\,{}_{n_1}\vec{k}_{n_3}$. In addition

$$\vec{x} = \left(R_B[\vec{q}|3]^t R_B[\vec{q}|3]\right)^{-1} R_B[\vec{q}|3]^t \, \vec{p}_B[\vec{q}|3]. \tag{D1}$$

Proof: $\left|R_B[\vec{q}|3]^t R_B[\vec{q}|3]\right|$, by direct evaluation, is trivial if and only if ${}_{n_1}\vec{k}_{n_2} = \pm\,{}_{n_1}\vec{k}_{n_3}$. □

Theorem 4: Let $R_\alpha = \mathrm{Rot}(\vec{k}_\alpha, \theta_\alpha)$, $R_\beta = \mathrm{Rot}(\vec{k}_\beta, \theta_\beta)$ and $R_\beta^{-1}R_\alpha = \mathrm{Rot}(\vec{k}_{\alpha\times\beta}, \theta_{\alpha\times\beta})$. Then $\mathcal{N}(R_\alpha, R_\beta) = 2\sin(|\theta_{\alpha\times\beta}|/2)$ and $\mathcal{A}(R_\alpha, R_\beta) = |\theta_{\alpha\times\beta}|$.

Proof: $\|(R_\alpha - R_\beta)\vec{e}\| = \|(R_\beta^{-1}R_\alpha\vec{e}) - \vec{e}\| = 2 \cdot |\sin(v) \cdot \sin(\theta_{\alpha\times\beta}/2)|$, where $v = \cos^{-1}(\vec{k}^t_{\alpha\times\beta}\,\vec{e})$. Thus, $\mathcal{N}(R_\alpha, R_\beta) = 2\sin(|\theta_{\alpha\times\beta}|/2)$. Since $(R_\alpha\vec{e})^t(R_\beta\vec{e}) = (R_\beta^{-1}R_\alpha\vec{e})^t\,\vec{e}$, $\mathcal{A}(R_\alpha, R_\beta) = |\theta_{\alpha\times\beta}|$. □

Appendix V
A Calibration Method for the Uncertainty Scale Factor s_x

The s_x factor as investigated by Lenz and Tsai [16] can be identified using a square template. First, put the template on an inspection table. Adjust the vision camera to be vertical to the template by trial and error and testing the following hypotheses:

$$\mathrm{H}_0: \; m_1 = m_3 \text{ and } m_2 = m_4$$

versus

$$\mathrm{H}_1: \; m_1 \neq m_3 \text{ or } m_2 \neq m_4$$

where m_i is the slope of edge L_i's image, and $L_1 \parallel L_3$ and $L_2 \parallel L_4$ are assigned.

It is noted that the measuring unit, either in inches or pixels, does not alter the test results.

Once passing the test, s_x is identified as follows:

$$s_x = \frac{\Delta x}{\Delta y} \cdot \frac{d_x}{d_y} \tag{E1}$$

where $\Delta x = x_{\max} - x_{\min}$, $x_{\min} \leq x_i \leq x_{\max}$, $i \in I_4$, $\Delta y = y_{\max} - y_{\min}$, $y_{\min} \leq y_i \leq y_{\max}$, $i \in I_4$, $(x_i, y_i)^t$, in pixels, are the coordinates of V_i's image, V_i is the i^{th} vertex of the square, and d_x and d_y, available in the camera manual, are the physical dimensions of a pixel.

Appendix VI
A Calibration Method of the Image Center Using Rectangular Patterns

Coordinates of the image center, i.e., $(c_x, c_y)^t$, can be identified by using either a 2-D rectangular or 3-D cuboid reference object. The necessary formulas are summarized below without derivations.

A. Reference Object: A Cube

Let $(\mu_x, \nu_x)^t$, $(\mu_y, \nu_y)^t$ and $(\mu_z, \nu_z)^t$, calculated from images of parallel edges as illustrated in Fig. 17, be the vanishing points of the reference object's body frame [37]. Then

$$\begin{bmatrix} c_x \\ c_y \end{bmatrix} = \begin{bmatrix} \mu_z - \mu_x & \nu_z - \nu_x \\ \mu_z - \mu_y & \nu_z - \nu_y \end{bmatrix}^{-1} \cdot \begin{bmatrix} \mu_y \cdot (\mu_z - \mu_x) + \nu_y \cdot (\nu_z - \nu_x) \\ \mu_x \cdot (\mu_z - \mu_y) + \nu_x \cdot (\nu_z - \nu_y) \end{bmatrix}. \tag{F1}$$

The calibration accuracy can be improved by taking more samples.

B. Reference Object: A 2-D Rectangle

A minimum of three samples is necessary. Take m samples and calculate vanishing points $(\mu_{x,i}, \nu_{x,i})^t$ and $(\mu_{y,i}, \nu_{y,i})^t$, where $m \geq 3$ and $i \in I_m$. Then, resolve c_x and c_y as follows:

$$\begin{bmatrix} c_x \\ c_y \end{bmatrix} = (C^tC)^{-1}\,C^t\vec{d} \tag{F2}$$

where

$$C = \begin{bmatrix} \mu_{x,2} + \mu_{y,2} - \mu_{x,1} - \mu_{y,1} & \nu_{x,2} + \nu_{y,2} - \nu_{x,1} - \nu_{y,1} \\ \vdots & \vdots \\ \mu_{x,m} + \mu_{y,m} - \mu_{x,m-1} - \mu_{y,m-1} & \nu_{x,m} + \nu_{y,m} - \nu_{x,m-1} - \nu_{y,m-1} \end{bmatrix}$$

$$\vec{d} = \begin{bmatrix} \mu_{x,2} \cdot \mu_{y,2} + \nu_{x,2} \cdot \nu_{y,2} - \mu_{x,1} \cdot \mu_{y,1} - \nu_{x,1} \cdot \nu_{y,1} \\ \vdots \\ \mu_{x,m} \cdot \mu_{y,m} + \nu_{x,m} \cdot \nu_{y,m} - \mu_{x,m-1} \cdot \mu_{y,m-1} - \nu_{x,m-1} \cdot \nu_{y,m-1} \end{bmatrix}.$$

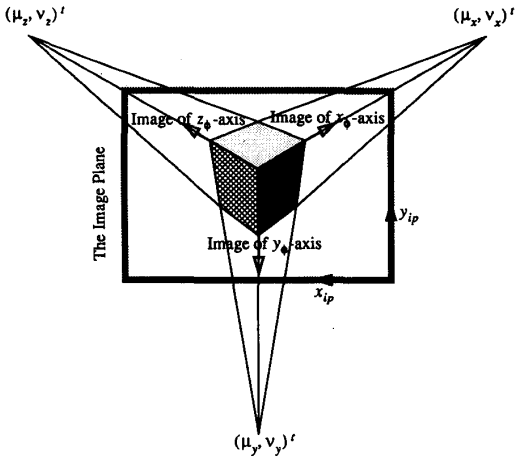

Fig. 17. Vanishing points of a cuboid body frame.

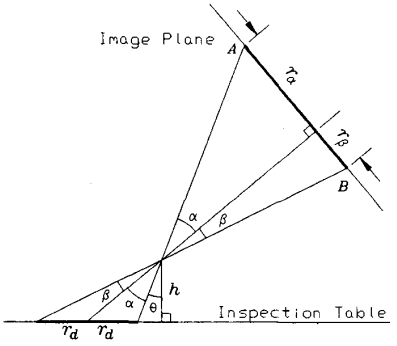

Fig. 18. Biased disk center on the image plane.

APPENDIX VII
BIASED RATIO OF THE DISK CENTER ON THE IMAGE PLANE

Without quantization and distortion errors, the pin-hole image of a circular disk is another circular disk when the disk plane is perpendicular to the optical axis. However, the boundary of the pin-hole image is not a regular ellipse when the disk plane is not perpendicular to the optical axis. Fig. 18 demonstrates the situation, where r_d is the disk radius. The biased ratio (r_β/r_α), as given by the following equation, equals unity if and only if the optical axis is perpendicular to the disk.

$$\frac{r_\beta}{r_\alpha} = \frac{\tan(\beta)}{\tan(\alpha)} \tag{G1}$$

where $\alpha = \tan^{-1}(r_d/h + \tan\theta) - \theta$ and $\beta = \tan^{-1}(2 \cdot r_d/h + \tan\theta) - \alpha - \theta$.

The biased ratio (r_β/r_α) is evaluated and plotted in Fig. 19 for $\theta = 15°$ and $60°$ over a range of $(h/r_d) \in [0.1, 30]$. It is observed that (r_α/r_β) converges to 1.0 as h/r_d increases. However, at $h = 30 \cdot r_d$ the biased ratio still deviates from the neutral value of 1.0 by about 2%. Therefore, using the mid-point of A and B to approximate the image of the disk center may introduce detectable bias where A and B, as marked in Fig. 18, are boundary points of the disk image.

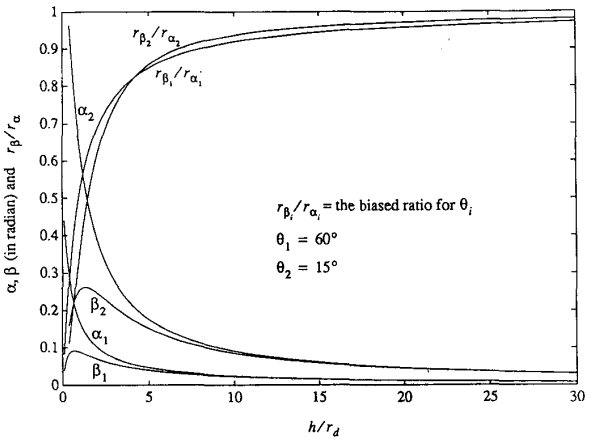

Fig. 19. View angles and biased ratios of a circular disk.

REFERENCES

[1] Y. I. Abdel-Aziz and H. M. Karara, "Direct linear transformation into object space coordinates in close-range photogrammetry," in *Proc. Symp. Close-Range Photogrammetry* (Univ. of Illinois, Urbana-Champaign, 1971), pp. 1–18.

[2] *Manual of Photogrammetry*, 4th ed. Bethesda, MD: Amer. Soc. of Photogrammetry, 1980.

[3] M. Born and E. Wolf, *Principles of Optics*. Oxford, England: Pergamon, 1965.

[4] D. C. Brown, "Close-range camera calibration," *Photogrammetr. Eng.*, vol. 37, pp. 855–866, 1971.

[5] C. H. Chen and A. C. Kak, "Modeling and calibration of a structural light scanner for 3-D robot vision," in *Proc. IEEE Int. Conf. Robotics Automat.*, 1987, pp. 807–815.

[6] A. Dainis and M. Juberts, "Accurate remote measurement of robot trajectory motion," in *Proc. IEEE Int.Conf. Robotics Automat.*, 1985, pp. 92–99.

[7] W. Faig, "Calibration of close-range photogrammetry systems: Mathematical formulation," *Photogrammetr. Eng.*, vol. 41, pp. 1479–1486, 1975.

[8] O. D. Faugeras and G. Toscani, "The calibration problem for stereo," in *Proc. IEEE Int. Conf. Comput. Vision Pattern Recognition*, 1986, pp. 15–20.

[9] M. Fischler and R. Bolles, "Random sample consensus: A paradigm for model fitting applications to image analysis and automated cartography," in *Proc. Image Understanding Workshop*, Apr. 1980, pp. 71–88.

[10] S. Ganapathy, "Decomposition of transformation matrices for robot vision," in *Proc. IEEE Int. Conf. Robotics Automat.*, 1984, pp. 130–139.

[11] D. B. Gennery, "Stereo-camera calibration," in *Proc. Image Understanding Workshop*, 1979, pp. 101–107.

[12] C. C. Geschke, "A system for programming and controlling sensor-based robot manipulators," *IEEE Trans. Pattern Anal. Machine Intell.*, vol. PAMI-5, no. 1, pp. 1–7, Jan. 1983.

[13] A. Izaguirre, P. Pu, and J. Summers, "A new development in camera calibration: Calibrating a pair of mobile cameras," *Int. J. Robotics Res.*, vol. 6, no. 3, pp. 104–116, 1987.

[14] R. A. Jarvis, "A perspective on range finding techniques for computer vision," *IEEE Trans. Pattern Anal. Machine Intell.*, vol. PAMI-5, no. 2, pp. 122–139, 1983.

[15] ——, "A laser time-of-flight range scanner for robotic vision," *IEEE Trans. Pattern Anal. Machine Intell.*, vol. PAMI-5, no. 5, pp. 505–512, 1983.

[16] R. K. Lenz and R. Y. Tsai, "Techniques for calibration of the scale factors and image center for high accuracy 3D machine meteorology," in *Proc. IEEE Int. Conf. Robotics Automat.*, 1987, pp. 68–75.

[17] P. Liang, Y. L. Chang, and S. Hackwood, "Adaptive self-calibration of vision-based robot systems," *IEEE Trans. Syst. Man Cybern.*, vol. 19, no. 4, pp. 811–824, July/Aug. 1989.

[18] Y. Liu, T. S. Huang, and O. D. Faugeras, "Determination of camera location from 2D to 3D line and point correspondences," in *Proc. IEEE Int. Conf. Computer Vision Pattern Recognition*, 1988, pp. 82–88.

[19] J. Y. S. Luh and J. A. Clasen, "A three-dimensional vision by off-self

system with multi-cameras," *IEEE Trans. Pattern Anal. Machine Intell.*, vol. PAMI-7, no. 1, pp. 35–45, Jan. 1985.
[20] ???? Malhotra, "A computer program for the calibration of close-range cameras," in *Proc. Symp. Close Range Photogrammetric Syst.* (Urbana, IL), 1971.
[21] P. Mansbach, "Calibration of a camera and light source by fitting to a physical model," *Computer Vision, Graphics, Image Processing*, vol. 35, pp. 200–219, 1986.
[22] H. A. Martins, J. R. Birk, and R. B. Kelley, "Camera models based on data from two calibration planes," *Computer Graphics Image Processing*, vol. 17, pp. 173–180, 1981.
[23] L. Matthies and S. A. Shafer, "Error modeling in stereo navigation," *IEEE J. Robotics Automat.*, vol. RA-3, no. 3, pp. 239–248, June 1987.
[24] M. Osada, "Development of visual feedback robots, designed to assemble complex automotive components," in *Crossing Bridges: Advances in Flexible Automation and Robotics*. New York: Amer. Soc. Mechanic. Eng., 1988, pp. 823–828.
[25] R. Paul, *Robot Manipulators*. Cambridge, MA: MIT Press, 1982.
[26] G. V. Puskorius and L. A. Feldkamp, "Global calibration of a robot/vision system," in *Proc. IEEE Int. Conf. Robotics Automat.*, 1987, pp. 190–195.
[27] S. A. Shafer, "Geometric camera calibration for machine vision systems," *Manufact. Eng.*, vol. 102, no. 3, pp. 85–88, Mar. 1989.
[28] K. Shirai and S. Uchida, "3-D measurement using automatic camera calibration method," in*Proc. IEEE Int. Conf. Computer Vision Pattern Recognition*, 1986, pp. 931–933.
[29] Y. C. Shiu and S. Ahmad, "Finding the mounting position of a sensor by solving a homogeneous transformation equation of the form $AX = XB$," *IEEE Trans. Robotics Automat.*, vol. 5, no. 1, pp. 16–28, Feb. 1989.
[30] I. Sobel, "On calibrating computer controlled cameras for perceiving 3-D scenes," *Artificial Intell.*, vol. 5, pp. 185–198, 1974.
[31] T. M. Strat, "Recovering the camera parameters from a transformation matrix," in *Proc. DARPA Image Understanding Workshop*, Oct. 1984, pp. 264–271.
[32] I. Sutherland, "Three-dimensional data input by tablet," *Proc. IEEE*, vol. 62, pp. 453–461, Apr. 1974.
[33] R. Y. Tsai, "A versatile camera calibration technique for high-accuracy 3D machine vision metrology using off-the-self TV cameras and lenses," *IEEE J. Robotics Automat.*, vol. RA-3, no. 4, pp. 323–344, Aug. 1987.
[34] R. Y. Tsai and R. K. Lenz, "A new technique for fully autonomous and efficient 3D robotics hand/eye calibration," *IEEE J. Robotics Automat.*, vol. 5, no. 3, pp. 345–358, June 1989.
[35] R. N. Vaishnav and E. B. Magrab, "A general procedure to evaluate robot positioning errors," *Int. J. Robotics Res.*, vol. 6, no. 1, pp. 59–74, Spring 1987.
[36] W. K. Veitschegger and C.-H. Wu, "Robot accuracy analysis based on kinematics," *IEEE J. Robotics Automat.*, vol. RA-2, no. 3, pp. 171–179, Sept. 1986.
[37] C.-C. Wang and K.-C. Lai, "Solving the cubic monocular pose problem by vanishing point method," in *Proc. 1st Int. Conf. Automat. Technol.*, July 4–6, 1990, pp. 215–224.
[38] P. R. Wolf, *Elements of Photogrammetry*. New York: McGraw-Hill, 1974.

Ching-Cheng Wang received the B.S. degree in physics from National Taiwan University, Taiwan, in 1974 and the M.S. degree in physics from Northwestern University, Evanston, IL, in 1978. He received the M.S. degree in applied statistics in 1979, the M.S. degree in operations research in 1980, and the Ph.D. degree in industrial engineering in 1983, all from the Georgia Institute of Technology, Atlanta.

He is currently an Associate Professor in the Department of Industrial Engineering and Information Systems at Northeastern University, Boston, MA. His primary areas of research interest are system identification, modeling, verification and calibration, and automated optical inspection and object recognition.